Title

ENHANCEMENT OP CRYOGENIC FRACTURE TOUGHNESS THROUGH MICROSTRUCTURAL CONTROL IN A FERRITIC Fe-12Ni-0.25Ti ALLOY SYSTEM

Author

Jin, Sungho.

Publication Date

1974-06-01

LBL-2789

ENHANCEMENT OF CRYOGENIC FRACTURE TOUGHNESS THROUGH MICROSTRUCTURAL CONTROL IN A FERRITIC Fe-12Ni-0.25Ti ALLOY SYSTEM

Sungho Jin
(Ph. D. thesis)

June 1974

Prepared for the U. S. Atomic Energy Commission
under Contract W-7405-ENG-48

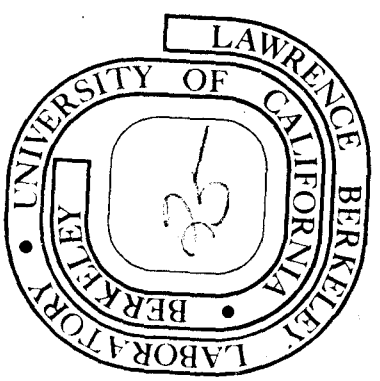

LBL-2789

DISCLAIMER

Table of Contents

ENHANCEMENT OF CRYOGENIC FRACTURE TOUGHNESS THROUGH MICROSTRUCTURAL CONTROL IN A FERRITIC Fe-12Ni-0.25Ti ALLOY SYSTEM

Sungho Jin

Inorganic Materials Research Division, Lawrence Berkeley Laboratory and Department of Materials Science and Engineering, College of Engineering; University of California, Berkeley, California

ABSTRACT

A thermal cycling technique which allows the grain refinement of Fe-12Ni-0.25Ti alloy from 40-60 μm (ASTM #5-6) to 0.5 - 2 μm (ASTM #15-18) in four cycles has been developed. The process consists of alternate annealing in γ range and (α + γ) range with intermediate air cooling. The transformation behavior, the change of microstructures and cryogenic mechanical properties on each cycling step are described.

Due to the ultrafine grain size, the ductile-brittle transition temperature of this completely ferritic alloy was suppressed below 6°K even in the presence of a sharp crack. Simple and economic methods of Charpy impact testing and fracture toughness testing below 6°K were developed using the styrofoam-lucite box system. In fracture toughness testing at 77°K, the mode of fracture was altered from brittle quasi-cleavage to complete ductile rupture through the grain refining. Fracture toughness testing of grain refined alloy at 6°K revealed essentially ductile dimple rupture. Cryogenic mechanical properties of Fe-Ni-Ti alloys were compared with two other commercial cryogenic alloys.

I. INTRODUCTION

The objective of this research is the design of new classes of cryogenic steels having combined strength and toughness at very low temperatures. Current engineering problems include the transport, storage and handling of liquified gas and the design of superconducting power systems and transmission lines. Available structural alloys tend to become brittle at low temperatures, posing design and safety problems which can be solved if new tough cryogenic alloys are made available.

Steels generally used for cryogenic service are limited in number. Austenitic alloys retain their high toughness down to very low temperature but their strength is rather low. Ferritic alloys become much stronger at cryogenic temperatures due to the large thermal component of yield strength but tend to become brittle, especially in the presence of a sharp crack. If the problem of the ductile-brittle transition can be overcome, ferritic alloys offer greater potential due to their higher strength.

The specific purpose of this work is to suppress or practically eliminate the D-B transition behavior of ferritic Fe-base alloys through the study and control of microstructures.

II. BASIC APPROACH

Cottrell[1] and Petch's[2] theoretical analysis based on dislocation theory, using the energy balance between the work done on moving dislocations and the surface energy produced by opening a crack, relates the ductile-brittle transition temperature to metallurgical parameters as follows.

$$T_c \propto \ln \left[\frac{B\, d^{1/2} K_y}{\beta G \gamma - K_y^2} \right] \quad . \ . \ . \qquad (1)$$

where T_c is the D-B transition temperature, d is the grain size, K_y is the Hall-Petch slope, G is the shear modulus, γ is the surface energy, and B and β are constants. The transition temperature of ferritic alloys, therefore, can be suppressed by 1) refining the grain size, 2) reducing the Petch slope, and 3) increasing the surface energy. These three variables are controllable through compositional and microstructural changes. The physical meanings of these variables are as follows. The grain size, d, represents the degree of local stress concentration at boundaries (dislocation pile-up length or mean-free slip path). The Petch slope, K_y, represents the resistance against slip propagation across the grain boundaries[3] (or the difficulty in relieving the local stress concentration at the boundaries), and is related to the impurity locking of the dislocation sources, number of available slip systems, and the ease of cross slip of dislocations. The surface energy, γ, in Eq. (1) is the sum of γ(thermodynamic) and γ(plastic deformation).

It can be increased by removing the boundary segregation of impurities[4] such as P, S, Sb etc., and also by preventing the formation of grain boundary films of brittle precipitates. Another possible way of lowering the transition temperature is by the introduction of small amounts of retained austenite. This aspect will be discussed in section IV-D.

A. Alloy Composition

An Fe-base alloy composition of nominally 12% Ni and 0.25% Ti with low impurity (S,P,etc.) content was used in this research. The small amount of titanium scavenges the interstitials (carbon and nitrogen), which is believed to reduce the Petch slope, resulting in a lower transition temperature. This point requires further investigation. Most of the Fe-base cryogenic alloys contain appreciable amounts of nickel. Nickel as well as other elements in the platinum group are known to suppress the transition temperature of ferritic alloys.[4] Several explanations have been suggested.[5]

1) Nickel enhances the cross slip of dislocations at low temperatures.
2) Nickel may have the effect of scavenging interstitials (i.e. decreasing the strength of dislocation pinning by interstitials).
3) Introduction of dislocated martensite by alloying iron with 8 - 25% nickel increase the mobile dislocation density.

Even though the main mechanism responsible has not been clearly identified, the beneficial effect of Ni on cryogenic toughness is well established.[4,6,7] Fe-Ni alloys are known to possess about the lowest value of Ky among the Fe-base alloys. According to Sasaki,[8] the Petch slope of Ti-scavenged Fe-12Ni-0.5Ti alloy is ~ 0.15 ksi/mm$^{-1/2}$ at 25°C and ~ 0.56 ksi/mm$^{-1/2}$ at - 196°C, which is considerably smaller than other steels.[9,10] This low value of Ky should be beneficial according to Cottrell-Petch's prediction (Eq. (1)).

B. Alloy Processing

With a given alloy composition, Eq. (1) reduces to

$$T_c = C_1 + C_2 \ln d^{1/2} \qquad (2)$$

where C_1 and C_2 are constants. Experimental work[4,11] also suggested other relationships like,

$$T_c = C_1 - C_2 d^{-1/2} \quad . \qquad (3)$$

Whatever the equation is, the dependence of transition temperature on grain size is clearly established.[12,13,8] Hence the major focus of this research has been on the design of processes which accomplish significant grain refinement.

Previous work[14-16] established two techniques for refining the grain size of Fe-Ni alloys of moderate nickel content. Following studies by Grange,[17] Porter and Dabkowski[14] demonstrated grain refinement through a thermal cycling procedure which included repeated cycles of rapid austenitizing and cooling. Grain size as small as 3-5μm (mean intercept length: ASTM #13-14) was obtained. Saul et al.[15] also observed grain refinement in maraging steels on simple repeated austenitizing (from ASTM #2 to #7 in 4 cycles). An alternate technique was used by Miller,[16] who reported ultrafine grain size (0.3-1.1 μm; ASTM #17-19) in an Fe-Ni alloy which had been severely cold-worked and then annealed in the two-phase ($\alpha + \gamma$) range.

In earlier work in this thesis project, variants of both these processing techniques were used on the alloy Fe-12Ni-0.25Ti. The results have been reported (ref. 18). Both techniques led to alloys of exceptional strength and ductility at cryogenic temperature. However, both processing techniques had undesirable features. When the cyclic austenitizing process was used, the grain size seemed to stabilize at 5-10 μm. A further improvement in low temperature ductility might be obtainable with finer grain size. A more refined structure can be achieved with mechanical working, but mechanical working is often an impractical or undesirable step in final alloy processing. Therefore an alternate thermal treatment which would accomplish a grain refinement comparable to that obtainable with mechanical work was sought.

III. TECHNICAL APPROACH

The technical approach leading to the grain refinement processes used here may be briefly described as follows: The Fe-12Ni-0.25Ti alloy is expected to show roughly the same transformation behavior as the Fe-12Ni binary alloy, because of the small amount of Ti present and its partial consumption in scavenging interstitials. Previous research on the transformation behavior of Fe-Ni alloys in this composition range (summarized, for example, by Floreen[19]) indicates that when these alloys are rapidly heated or cooled between room temperature and the γ-field both the $\alpha \rightarrow \gamma$ and the $\gamma \rightarrow \alpha$ transformations occur primarily through a diffusionless shear mechanism, while if the alloys are annealed within the two phase ($\alpha + \gamma$) field the transformation proceeds through a diffusional nucleation and growth process leading to an equilibrium partitioning of nickel between the two phases. Either transformation mechanism may be used for grain refinement. If α is heated to the γ-field and then cooled to room temperature, a decrease in apparent grain size (or martensite packet size) results, presumably to relieve the internal strain built up during the shear transformation.[15] If α is annealed inside the two phase region a very fine lath-like structure results, presumably from preferential γ nucleation in the boundaries of the martensite plates.[16]

The fine lath-like structure obtained after two-phase anneal is, however, not a desirable structure for high toughness, and may even cause a decrease in toughness due to easy crack propagation

parallel to the laths. In Miller's research[16] the stored energy of prior cold work seemed effective in destroying the preferential alignment of those laths. It seems plausible that residual strain from a cyclic shear transformation may accomplish the same effect, particularly if the strain is allowed to accumulate through repeated cycling.

This research, therefore, has been concentrated on thermal cycling treatments of the type illustrated schematically in Fig. 1 (the Fe-Ni equilibrium phase diagram was obtained from Hansen[20]) in which austenite reversions are alternated with two-phase decompositions. The annealing temperatures were chosen from the results of dilatometric studies of the kinetics of the phase transformations, with the guiding principle that the austenitizing temperature should be low, to minimize grain growth, while the two-phase decomposition temperature should be high, to maximize the rate of decomposition. The annealing times and total number of cycles were chosen from metallographic studies of grain refinement and low-temperature mechanical tests of the resulting alloys.

IV. DISCUSSIONS ON PROCESS OF GRAIN REFINEMENT

A. Materials Preparation

A low carbon alloy of nominal composition Fe-12Ni-0.25Ti was obtained from pure starting materials (99.9% purity) by induction melting in an inert gas atmosphere. Two twenty pound ingots of 2.75 in. (7.0 cm) diameter were prepared by slow casting in a rotating copper chill mold. Ingot composition was determined to be (in weight percent): 12.07 Ni, 0.26 Ti, 0.001 C, 0.014 N, 0.003 P, 0.004 S, with the balance Fe. The ingots were homogenized under vacuum at 1050°C for 120 hours, cross-forged at ~1100°C to thick plates 4 in. (10.2 cm) wide by 0.75 in. (1.9 cm) thick, then air-cooled to room temperature. The plates were then annealed at 900°C for two hours to remove most of the prior deformation strain and air cooled to room temperature. This final anneal was included to establish a standard initial state for research purposes; earlier work[18] has shown that the processed alloys have somewhat better cryogenic mechanical properties when grain refined directly from the as-forged condition.

B. Phase Transformation Studies

Iron and nickel form two types of solid solutions, i.e., α(BCC) and γ(FCC). Over a wide range of compositions and temperatures, Fe-Ni alloys in equilibrium consist of a mixture of the two phases as shown in Fig. 1. On isothermal holding for a long enough time to reach the equilibrium, the transformation obeys this phase diagram.

On continuous heating or cooling, however, the phase transformation follows the metastable diagram rather than the equilibrium phase diagram. Therefore, in a complicated thermal cycling which involves both continuous and isothermal heat treatment, the phase transformation behavior can not be easily predicted. As the nickel content varies from 0 to ~30%, Fe-Ni base alloys quenched from the austenite range show three different structural features as Owen et al.[21] reported. From 0 to ~8% Ni, they show equiaxed ferrite structures, from ~10 to ~25% Ni dislocated martensite, and above 25% Ni twinned martensite. The present alloy system falls in the category of dislocated martensite, as is the case of maraging steels. Typical transmission-electron micrographs of the Fe-12Ni-0.25Ti alloy (simple-austenized and cooled), Figs. 2 and 3, confirms the dislocated martensite type structure. Extensive research has been done on phase transformation behavior and microstructures of the Fe-Ni system and many classes of maraging steels. The generally accepted view is that when these alloy systems (containing 10-25% Ni) are heated or cooled continuously between room temperature and γ range, the phase transformation occurs by a diffusionless shear mechanism, while if they are annealed within the two phase range, the transformation occurs by a diffusional process to reach the equilibrium alloy partitioning.

Dilatometric studies were conducted to determine phase transformation kinetics in this alloy. Tube-shaped dilatometry specimens 1.5 in. (3.8 cm) long and 0.25 in. (0.64 cm) in diameter

with 0.04 in. (0.1 cm) wall thickness were machined from the annealed starting material. Temperatures were monitored with a chromel-alumel thermocouple spot welded at the mid-point of the specimen length. The experiments were carried out with heating and cooling rates of approximately 15°C/min., roughly duplicating the rates used in the heat treatment of the alloy.

Sample dilatometric curves are given in Fig. 4. Figure 4(a) illustrates transformation behavior when an α(martensite) is continuously heated into the γ region, then cooled to room temperature. Reversion to austenite begins at a temperature slightly below the maximum in the dilation curve at 673°C (which we have taken as a measure of the austenite start temperature, A_s) and is completed at a temperature slightly above the minimum in the curve at 715°C (which measures the austenite finish temperature, A_f). On cooling, the martensite transformation begins near 473°C (M_s) and is largely complete by 412°C (M_f). On cycling, the sample undergoes a small permanent set, measured by the offset in the cooling curve at low-temperature. This offset results from transformation strain of the sample and does not signify the presence of retained austenite; no austenite is detected in x-ray studies of samples cycled back to room temperature. Figure 4(a) suggests an austenitizing temperature of about 730°C to insure that the transformation is completed, and a maximum two-phase decomposition temperature of about 650°C to insure that shear reversion has not become significant.

Dilatometric curves monitoring isothermal decomposition at 650°C are shown in Fig. 4(b). The M_s temperature is essentially independent of transformation time ($t \geq 30$ min.) indicating that the nickel content of the γ formed is essentailly independent of the γ volume fraction. This γ apparently transforms completely to α on cooling; no retained austenite is detected in x-ray diffraction analyses of samples cooled to room temperature. (Retained austenite was detected, however, after decomposition at temperatures < 600°C).

Given the curves in Fig. 4(b) we can phrase a rough estimate of the rate of decomposition which is useful in selecting an annealing time. If we assume that the dilation is a linear function of the fraction transformed and estimate the dilation on complete transformation from the total offset in the curves of Fig. 4(a), we obtain the estimated isothermal transformation curve shown in Fig. 5. This curve has an asymptote indicating equilibrium with slightly more than 80% γ, which agrees roughly with an estimate based on the Fe-Ni binary phase diagram. It is inferred from Fig. 5 that an annealing time of 2 hours at 650°C will yield a product which is roughly 60% γ, providing an overall grain refinement near the optimum. This estimate is supported by the metallographic results given below.

If the 730°C/650°C cycle is repeated after decomposition at 650°C, the kinetics of transformtion are complicated by the inhomogeneous distribution of nickel throughout the microstructure. The change of phase transformation temperatures on this alternate thermal cycling is given in Table I. A sample annealed for two hours

at 650°C will consist of roughly 60% γ of composition ~13% Ni (estimated from the Fe-Ni binary phase diagram) together with ~40% residual α of mean nickel concentration near 10% (well above the equilibrium at ~4% Ni) which may be heterogeneously distributed. If the material is air cooled to room temperature and then reheated to 730°C regions of different Ni concentration will transform at different temperatures (and perhaps by different mechanisms) leading to the more complex transformation behavior illustrated by the dilatometer trace shown in Fig. 6. It nonetheless appears that the pronounced shear reversion is essentially complete at 730°C.

Transformation behavior on subsequent cooling depends on the extent of homogenization at 730°C, and hence on the time of anneal, as illustrated by curves (b) and (c) of Fig. 6. An anneal of 2 hours at 730°C is not sufficient to homogenize the alloy. The continued presence of regions of relatively high Ni concentration is indicated by the suppression of the A_s temperature on reheating (curve (d) of Fig. 6). However, after the second 2 hour anneal at 730°C the A_s temperature in the next heating lies above 650°C, indicating that shear reversion to γ does not become pronounced until the temperature is raised above 650°C.

C. Microstructural Changes on Cycling

On the basis of dilatometric and microstructural studies a grain refining process consisting of alternate two-hour anneals at 730°C and 650°C was selected. A four-cycle process is shown

schematically in Fig. 1, where the successive steps are labelled 1A (730°C), 1B (650°C), 2A (730°C) and 2B (650°C). The evolution of the microstructure during this cycling is illustrated by the optical micrographs given in Fig. 7 and by the scanning electron micrographs in Fig. 8. After final cycle 2B the bulk of the microstructure consists of a fine mixture of platelet grains approximately 1-4 microns long and a fraction of a micron in the short dimension. The preferential orientation of these grains has been largely eliminated. The general features of the grain refinement process are apparent in Fig. 7 and Fig. 8. Figure 7(a) shows the microstructure of the annealed starting material. The apparent grain size is 40-60 μm (ASTM #5-6). After cycle 1A the apparent grain size (Fig. 7(b)) has reduced to ~15 μm (ASTM #9). These grains consist of blocky laths of dislocated martensite as shown in Figs. 2 and 3. During cycle 1B the martensite is isothermally decomposed to give the microstructure shown in Fig. 7(c) and in Fig. 8(a). From the microstructure it appears that the austenite transformation begins along prior austenite grain boundaries, and the austenite then grows into the grains along what appear to be the prior martensite lath boundaries. After two hours the microstructure consists of a fine admixture of α with γ as platelets or lath shaped particles within grains, and with γ in a more blocky form along the prior grain boundaries. The γ then transforms to α on cooling to room temperature.

The microstructure after cycle 1B is not a desirable one for low temperature toughness. The strong preferential orientation of the microstructural features provides potential paths for easy crack propagation. This preferential orientation is largely removed during the second 730°C/650°C cyclic treatment.

The microstructure after cycle 2A is shown in Fig. 7(d) and Fig. 8(b). The evident microstructural changes are two. First, an homogenization reaction initiates along lath packet boundaries in the microstructure 1B, giving rise to the network of the white regions in Fig. 7(d). Second, there is some decomposition of the aligned laths of the 1B structure.

The interpretation of these features seems straightforward. On heating, the high nickel laths should revert to γ, giving rise to the first peak in the dilatometer trace in Fig. 6(b). At slightly higher temperature the low Ni matrix will begin to transform, causing the discontinuity in the slope of the dilatometer trace in Fig. 6(b). At 730°C the initial microstructure should consist of a mixture of high-nickel and lower nickel γ, with a possible admixture of retained α in the low nickel regions. This structure is unstable because of the heterogenous nickel concentration and will tend to homogenize. It cannot homogenize by simple diffusion because of the low bulk diffusivity of Ni in γ iron at this temperature and concentration[22] (the mean diffusion distance for Ni in γ, $(2Dt)^{1/2}$, is ~0.05 μm after two hours at 730°C). However, nucleated homogeneous γ can grow perpendicular to the platelet planes through interface diffusion of

nickel. Interface diffusion can also cause some decomposition of the individual platelets; however the bulk of the material within grains retains an oriented platelet morphology.

The oriented substructure of the alloy is broken up during the next two-phase decomposition, cycle 2B. The resulting microstructure is shown in Fig. 7(e) and in Fig. 8(c). Platelet orientation within grains is largely destroyed by the nucleation and growth transformation, and an ultrafine grained microstructure results. The network of homogenized material in the 2A microstructure also decomposes on a finer scale. The resulting grain size (0.5-2.0 μm; ASTM #15-18) is considerably below the best that is obtainable with simple cyclic austenitizing treatments and is comparable to that Miller[16] obtained after severe cold working.

The grain-refined alloy is apparently completely ferritic. No retained austenite was detected using conventional x-ray techniques. R. L. Miller[23] confirmed this result using a modification of his reported techniques[24,25] which permits detection of as little as 0.1% retained austenite.

The effect of adding additional 730°C/650°C cycles has also been explored. These do give an apparent additional refinement of the larger grains remaining in the microstructure, but the effect is small and has no obvious influence on cryogenic mechanical properties.

D. Formation of Retained Austenite

The effect of retained austenite formed during the reheating of martensite is somewhat contradictory in the literature.[26-29] However many examples of beneficial effects of small amounts of retained austenite on the mechanical properties have been reported.[30-32] The possibility of introducing stable retained austenite in a thermally grain refined Fe-12Ni-0.25Ti alloy, and its effect on cryogenic toughness was investigated.

Figure 9 shows the dilation-temperature curve obtained during the isothermal holding at different temperatures within the ($\alpha + \gamma$) two phase range. Holding time was held fixed for 2 hours. After decomposition at temperatures below 600°C, the γ phase formed does not completely transform back to martensite. This phenomenon becomes more pronounced as the holding temperature is lowered. The γ phase produced on 550° decomposition did not show any sign of transformation on cooling to room temperature, implicating the presence of the retained austenite. Since the present alloy is for use at cryogenic temperatures, specimen with an additional 550°C/2 hours treatment had been refrigerated at liquid nitrogen temperature before the analysis of retained austenite was conducted.

Quantitative measurement of the amount of the retained austenite was made using a Picker X-ray diffractometer with a CuK_α source. This X-ray analysis is based on the principle that the intensity of the diffracted beam is proportional to the volume fraction of the

diffracting phase. In the mixture of martensite and austenite, the retained austenite crystallites are usually distorted by the increase in specific volume when martensite forms, which results in a considerable decrease in the peak height. Also, a line broadening problem may arise. However, the integrated intensity, which is a measure of the total diffracted energy, is essentially independent of the lattice distortion and particle size. The equation suggested by Miller[24] was used in calculating the amount of retained austenite.

$$V_\gamma = \frac{1.4\ I_\gamma}{I_\alpha + 1.4\ I_\gamma} \qquad (4)$$

where V_γ is the volume fraction of austenite, I_γ is the average of the integrated intensity from the $(220)_\gamma$ and $(311)_\gamma$ peaks and I_α is the integrated intensity from the $(211)_\alpha$ peak. According to this analysis, the amount of retained austenite, in a specimen which was grain refined (by 8 cycles) and annealed at 550°C for 2 hours, was found to be approximately 3-5 volume %. This retained austenite remained stable down to liquid nitrogen temperature. No retained austenite was detected in specimens without the 550°C anneal.

Transmission electron microscopy was used to investigate the presence of retained austenite and its distribution. All specimens were refrigerated at 77°K before thin foil preparation. The diffraction patterns of specimen 1A (Figs. 2 and 3) do not show any FCC spots, and therefore there is no retained austenite in this specimen. This is consistent with the X-ray analysis. Figure 10 shows

a typical microstructure after grain refinement and 550°C anneal. Diffraction patterns, bright field and corresponding dark field electron micrographs are shown in Figs. 11 and 12. The dark field photograph was taken from the $(200)_\gamma$ spot in the diffraction pattern which was analyzed using the lattice constant $(a_o)_{bcc}$ = 2.8644 Å, $(a_o)_{fcc}$ = 3.5733 Å, and a camera constant λL = 3.8 cm·Å for Hitachi HU125 at 100 KV. Figures 11 and 12 clearly show that small crystallites of retained austenite are distributed along the grain or subgrain boundaries. Preliminary results of impact testing at 77°K and 6°K indicate that the introduction of 3-5% retained austenite by the 550°C treatment increases the Charpy impact energy of the grain refined alloy by at least 40-50 ft.lb. Investigation of the effect of retained austenite on cryogenic fracture toughness is continuing.[33]

V. MECHANICAL PROPERTIES AT CRYOGENIC TEMPERATURES

The mechanical test specimens were taken from the material prepared as described in section IV-A. The annealed 0.75 in. (1.9 cm) thick plates were cut into pieces 2.75 in. (7.0 cm) long. These pieces were then given selected thermal processing. After processing, one fracture toughness specimen and two Charpy impact specimens were machined from each piece along the longitudinal direction of forging, ensuring the same heat treatment for both tests. Tensile specimens (transverse direction) were obtained from the far end of the broken fracture toughness specimens. For comparison, the mechanical properties of two commercial cryogenic steels, i.e., 9 Ni steel and 304 stainless steel were also evaluated and included in the following results.

A. Cryogenic Tensile Properties

Tensile tests were conducted both at liquid nitrogen and liquid helium temperature using an Instron machine equipped with a cryostat. Subsize specimens of 0.5 in. (1.27 cm) gauge length and 0.125 in (0.32 cm) diameter were tested at a crosshead speed of 0.02 in./minute (0.05 cm/minute). Two specimens were tested at each stage of the cycling treatment. The deviation in yield strength between tests was ~5 ksi (35 newton/m^2). The stress-strain curves at 77°K and at 4.2°K are shown in Fig. 13. The serrated yielding behavior at liquid helium temperature is frequently observed in many alloy systems including most of the Fe-base alloys. Among the several suggested explanations,[34] i.e., 1) twinning, 2) martensite formation, 3) burst

type formation of dislocations and 4) adiabatic heating during the deformation,[35] the last appears to be the most probable reason for the discontinuous yielding of Fe-12Ni-0.25 Ti alloys. Both specimen 1A and 2B of Fe-12Ni-0.25Ti alloys were completely martensitic before testing, and no evidence of twinning was observed. Each step of discontinuous yielding was accompanied by a sudden rise of the specimen temperature.

The results of the tensile tests at 77°K are shown in Table II. The yield strength of Fe-12Ni-0.25Ti alloys at 77°K is in the range 140-150 ksi ($9.66\text{-}10.25\times10^8$ newton/m^2) and is rather insensitive to microstructure. The samples treated to stages 1B and 2B have slightly higher yield strength and lower tensile ductility than those at states 1A and 2A. These minor effects appear to be due to the precipitation of Ni_3Ti in the α phase at 650°C. The results of the tensile tests at 4.2°K are given in Table II. At liquid helium temperature, a considerable increase in yield strength was observed (185 - 200 ksi). It has been suggested by Conrad[36] that thermally activated overcoming of the Peierls-Nabarro stress is the mechanism responsible for the large thermal component of yield stress in BCC metals and alloys.

B. Cryogenic Impact Properties

1. Development of Testing Method

Charpy V-notch impact tests were conducted at liquid nitrogen temperature (77°K) using ASTM standard techniques,[37] and near liquid helium temperature (5-6°K), using a method recently developed in this laboratory.[38]

Impact testing at temperatures down to 77°K (liquid nitrogen temperature) is routinely accomplished according to ASTM specifications. The specimen is transferred in open air from a liquid bath to the test machine anvil and the pendulum is released within five seconds. However, this method is impractical at lower tempeatures since the low heat capacity of the metal leads to a rapid increase in specimen temperature during transfer.

To obtain valid low-temperature data DeSisto[39] designed an apparatus consisting of an evacuated enclosure which houses both an impact machine and an automatic feed mechanism which rapidly inserts specimens cooled in liquid helium into the test machine anvil. He was able to obtain data at instantaneous sample temperatures near 8°K. In other work Keifer, et al.[40] employed a glove-box arrangement to manually transfer specimens from an open-mouth dewar of liquid hydrogen to the test machine under inert atmosphere. They report test temperatures near 25°K when tested within 2 seconds.

While these techniques have permitted impact testing at low temperature, the elaborate apparatus required makes them impractical

for use in many laboratories, including our own. Therefore, a new and simple method to employ in current research on the design of tough alloys for cryogenic use was sought. Since this research concentrates on alloys of body centered cubic structure whose mechanical properties are typically sharp functions of temperature in the cryogenic region, it was required that the test technique allow close temperature control and insure the absence of appreciable thermal gradients in the specimen at the moment of impact.

The approach was to encase the test samples within individual insulating boxes which retain a controlled sample temperature near liquid helium temperature during the impact test. The requirements for a suitable boxing arrangement are that it must be an efficient insulator which withstands cooling to liquid helium temperature but contributes negligibly to the measured Charpy energies. These requirements seem well satisfied by employing a thin-walled lucite box insulated with open cell styrofoam which is continuously bathed with liquid helium. The test procedure and its calibration are discussed in the following sections.

a. Experimental method

A Charpy V-notch specimen is wrapped with open-cell styrofoam which is grooved along the specimen length direction to allow an easy passage of liquid helium (Fig. 14). The styrofoam surface is then wrapped with Scotch tape. The insulated specimen is then inserted into a rectangular lucite box (with one or two faces open) of 1/32 in. (0.8 mm) wall thickness having two 5/16 in. (7.9 mm) diameter

holes (Fig. 15). The cover for the open face is glued to the box system with Ethylene Dichloride solution. The Scotch tape and the styrofoam layer underneath the 5/16 in. (7.9 mm) holes are removed. A polyethylene inlet pipe of 3/8 in. (9.5 mm) I.D. and 1/2 in. (12.7 mm) length is glued to the box by Duco Cement. A lucite outlet pipe of 3/8 in. (9.5 mm) I.D. and 1 in. (25.4 mm) length is attached with Ethylene Dichloride solution.

This box system is placed on the anvil of a Charpy test machine. Liquid helium is transferred to the system through the inlet pipe from a pressurized dewar using an ordinary vacuum-insulated transferline. The pressure inside the dewar is maintained at around 2-3 psi ($1.4 \sim 2.1 \times 10^4$ newton/m^2) by an external supply of helium gas. Figure 16 is an illustration of the method. In Fig. 17, the liquid helium is being transferred to the box system located on the test machine anvil. A specimen temperature of 5-6°K is quickly attained and maintained as long as the liquid helium is transferred. Given proper assembly, the lucite box does not crack during liquid helium transfer. The liquid helium flows easily through the system and can be observed through the box wall. The released pendulum breaks the whole system. When the system is struck the weak bond at the base of the polyethylene inlet pipe fractures, thus ensuring the safety of the helium transfer line.

The open cell styrofoam layer has two functions. It absorbs the difference in thermal contraction between the lucite box and the specimen on cooling to liquid helium temperature, thereby preventing cracking of the box and escape of liquid helium. It also allows the

interstitial flow of liquid helium around the specimen for maximum cooling efficiency. After steady state is reached, a layer of liquid helium surrounds the metal specimen. Moreover, the insulated lucite box is extremely brittle at liquid helium temperature and absorbs very little energy during testing.

Because of the restricted space in the anvil of our test machine, the specimen legnth was reduced to 2.01 in. (51 mm) from the ASTM standard 2.17 in. (55 mm) length. However, the shortened length does not seem to introduce appreciable error. If the anvil were modified to allow larger specimens, a full size specimen could be used.

b. Temperature calibration

The specimen temperature was measured as a function of time using the following procedure.

A 0.1 in. (2.5 mm) diameter by 0.2 in. (5.1 mm) deep hole was drilled in the calibration specimen, and a 0.125 in. (3.2 mm) diameter by 0.5 in. (12.7 mm) long section of brass tubing was silver soldered over the hole to act as a collar to keep liquid helium away from the monitoring thermocouple (as shown in Fig. 15). For specimens that were actually impacted, plastic tubings of the same size were glued to the specimen. The insulating spacer and the box were then assembled around the specimen. A thermocouple (Au+0.07 %Fe - Chromel) was inserted into the drilled hole so that its tip was in good contact with the specimen. The thermocouple was then glued to the brass tube and the brass tube sealed to the lucite box to prevent escape of

liquid helium. This configuration ensures that the thermocouple measures the temperature at the centerline of the specimen rather than that of the bath of liquid helium in which the specimen is immersed.

A typical temperature time curve obtained using a dewar pressure of 2-3 psi ($1.4\sim2.1\times10^4$ newton/m^2) during transfer is shown in Fig. 18. Liquid helium transfer is initiated at t=0. Between t=0 and t_1, liquid helium is consumed in cooling the transfer line and does not significantly affect the specimen temperature. At t_1 liquid helium begins to cool the box system. The specimen temperature drops to below 6°K in about 60-80 seconds. It then remains constant for as long as liquid helium is transferred. At t_2 the hissing sound of the evaporated helium gas stops and liquid helium starts to come out of the outlet pipe. This evident change may be used as a sign that the test temperature has been reached. The pendulum may then be released. The specimen remains at 5-6°K until impact.

After testing, the helium transfer is halted and the next specimen set up for impacting. The transfer line consumes very little helium for its cooling after the first test. Liquid helium consumption for the first test is approximately 5-6 liters ($5\sim6\times10^{-3}$ m^3). In continuous operation each subsequent test consumes 2-3 liters ($2\sim3\times10^{-3}m^3$) of liquid helium.

Specimen temperatures both at point A and B in Fig. 15 (each point is approximately one-fourth of the sepcimen length apart from the notch) were measured. At the dewar pressure of 2-3 psi ($1.4\sim2.1\times10^4$ newton/m^2), the temperature gradient was hardly noticeable. However, at below 1 psi (0.7×10^4 newton/m^2) the temperature at A was several degrees higher than that at B. Therefore, it is necessary to keep the dewar pressure above a certain level to maintain a uniform specimen temperature.

c. Impact test calibration

There are two principal sources of error in the proposed impact test technique: a positive error introduced by the lucite box and styrofoam layer, and a negative error due to the shortened specimen length. Both errors appear to be small.

Plastics such as lucite are usually very brittle at low temperatures. Several tests at liquid helium temperature were made with the packing system without the metal specimen inside, and the impact energy absorbed by the lucite box and the styrofoam spacer was less than 1 ft-lb (1.36 newton/m). When a box system with a specimen inside is impacted, the face of the lucite box which is behind the specimen is crushed, and this also will contribute a small positive error.

Unless the anvil of the test machine is modified, the specimen length must be shortened from 12.17 in. (55 mm) to 2.01 in. (51 mm). For very tough alloys this shortened length may introduce a negative error in the measured impact energy because the maximum possible angle of bend is decreased.

For the purpose of calibration, 17 specimens of commercial 304 stainless steel with 2.17 in. (55 mm) length were tested at liquid nitrogen temperature according to the ASTM specification (open-mouth transfer). Another 17 specimens of the same material with 2.01 in. (51 mm) length were tested inside the lucite box system by transferring liquid nitrogen to the box. The results are compared in Table IV. The difference in the average impact energy obtained by these two methods was 3.6 ft-lbs. (4.9 newton-m) (approximately 3% of the average energy of this material), which was much less than the average scattering of the test data. The standard deviation of data obtained using the ASTM standard method was 8.7 ft-lbs (11.5 newton-m). Less extensive comparison tests with other cryogenic steels also showed good agreement between the standard and the proposed methods.

The small deviation in average impact energy between the standard and the proposed method seems principally due to the difference in specimens length. This error may decrease if the anvil of the impact machine is adjusted to accommodate a 2.17 in. (55 mm) boxed specimen. The increased scatter of data obtained with the proposed method was anticipated since the boxing arrangement introduces additional variables and since it is difficult to ensure that the notch in the boxed specimen is well centered in the anvil. Given that the Charpy impact test is at best a semiquantitative measure of the toughness of a material, the mechanical accuracy of the proposed test method seems reasonable.

The suggested test method has been used routinely in research on cryogenic alloys current at Berkeley. It offers two principal advantages. First, the tests are inexpensive and may be performed on any available impact machine whose specimen holder will accommodate the boxed specimen. Secondly, the method allows maintenance of a steady, uniform sample temperature of 5-6°K and avoids thermal gradients induced by sample transfer to the anvil.

2. Results of Charpy V-notch Impact Tests

Two specimens were tested at each condition. The results of these tests are presented in Table V. The broken specimens are shown in Fig. 19.

At 77°K all four structures showed high toughness. However, at 6°K specimens 1A and 1B were brittle. Fractographs taken at the center of the fracture surface in these specimens revealed a quasi-cleavage fracture mode. Specimens 2A and 2B remained tough at 6°K; the transition temperatures in Charpy testing for the bcc structures 2A and 2B are below this temperature.

C. Cryogenic Fracture Toughness

1. Fracture Toughness at 77°K

Fracture toughness tests at 77°K were conducted on an MTS machine equipped with a liquid nitrogen cryostat. Compact tension (WOL) specimens of 0.70 in. (1.78 cm) thickness were prepared and fatigue precracked according to ASTM specifications.[41] Two specimens were tested at each stage of the thermal cycling treatment.

The results of these tests are shown in Fig. 20. With the possible exception of sample 1B, these specimens were well away from plane strain conditions; a value of $K_Q \sim 140$ ksi $\cdot \sqrt{\text{in.}}$ was computed from the load-crack opening displacement (COD) curves.[41] At stages 1A, 1B, and 2A the alloy exhibited unstable crack propagation as marked by the dotted lines in the load-COD curves. Specimen 1B whose microstructure contained elongated laths showed the lowest fracture toughness ($K_Q \sim 100$ ksi $\cdot \sqrt{\text{in.}}$). Specimen 2A which contained a mixture of fine grains and large grains showed higher toughness than 1A and 1B, and the crack was repeatedly arrested but the unstable crack propagation could not be completely eliminated. However the fine-grained alloy 2B seemed immune to unstable crack propagation. The specimen was fully plastic, and the pre-induced crack grew slowly in a stable manner until the test was stopped.

The ASTM specification does not provide an appropriate method of fracture toughness evaluation for very tough or completely plastic materials. The approximate fracture toughness of specimen 2B was calculated based on the concept of work of fracture, using the integral over the area under the load-COD curve (Fig. 20). In this approach the

total work involved in fracture is measured and divided by the fracture area to obtain the strain energy release rate, g_C. Crack opening displacement measured by a clip gauge was calibrated to the value corresponding to that at the load point. The total area under the curve, ~5,300 in.-lb, divided by total fracture area, 0.7 in.^{2} gives g_C of ~ 7.500 in.-lb/in.^{2}. Using the equivalence relationship between the energy and the stress intensity factor, an approach in fracture mechanics derived by Irwin,[42] $g_C = K_{IC}^2/E$ (for plane stress) or $g_C = K_{IC}^2(1-\nu^2)/E$ (for plane strain), the fracture toughness of the specimen 2B at 77°K was calculated to be approximately $K_C \approx$ 470-500 ksi $\sqrt{in.}$ It should be remembered, however, that this calculation is not a valid and accepted one. The tests were not in the plane strain condition, and also plastic deformation accompanied the slow crack growth. Recent development in J-integral concept[43-45] may be useful for the toughness evaluation of the specimen 2B. The post-test fracture toughness specimens are compared to one another in Fig. 21. The brittleness of specimens 1A and 1B, the repeated crack arrest in specimen 2A, and the ductility of specimen 2B are visually apparent.

The fracture surfaces were examined by Jeolco JSM-U3 scanning electron microscope. Figure 22 shows scanning electron fractographs taken slightly ahead of the pre-induced fatigue crack along the center line of the sample. Specimens processed to stages 1A and 1B propagated fracture in a quasi-cleavage mode. At stage 2A, the fracture mode was a mixture of quasi-cleavage and ductile rupture. Fully grain refined specimens (2B) showed ductile dimple rupture over the whole fracture surface.

The enormous ductility of specimen 2B at 77°K was attributed principally to grain refinement because of the following facts.

1) The tensile ductility rather decreased due to the grain refining process (Tables II and III), which eliminates the possibility of other mechanisms of ductility enhancement, like increased density of mobile dislocations.

2) No retained austenite was detected after grain refining treatment.

It would be more correct to say that the toughness of this alloy was maintained rather than improved at cryogenic temperatures by grain refinement.

Commercial 9-Ni steel and type 304 stainless steel of the same specimen dimensions were also tested at 77°K. The results are shown in Fig. 23 and Fig. 24 (a) together with the results of the specimen 1A and 2B of the Fe-Ni-Ti alloy. Fracture toughness values are summarized in Table VI. The 9-Ni steel and Fe-Ni-Ti(1A) showed high impact energy (Table V) in Charpy tests at 77°K, their fracture surface revealing 100% ductile dimple mode. However, in fracture toughness testing in which a sharp fatigue crack was preinduced, these specimens failed by unstable crack propagation and their fracture surface showed brittle quasi-cleavage fracture mode. Specimen 2B which showed lower values of Charpy impact energy than 1A remained tough in the fracture toughness testing at 77°K. From these results it is clear that Charpy V-notch impact testing underestimates the ductile-brittle transition temperature.

2. Fracture Toughness at 6°K

Fracture toughness tests of Fe-Ni-Ti(1A), Fe-Ni-Ti(2B), 9-Ni steel and austenitic 304 stainless steel at liquid helium temperature were conducted using a method recently developed in this laboratory.[46] A similar "boxing technique" as that used in Charpy impact testing was employed. An oversize grip was used to provide space for an insulating box system which surrounded the specimen. Pins were made of grain-refined Fe-12Ni-0.25Ti alloy. At a dewar pressure of 5-6 psi, specimen temperature of 5-6°K was obtained in less than 3-4 minutes and maintained during the tests. The insulating box system remained intact without cracking until the test was finished. Figures 25 through Fig. 29 illustrate this method.

The results of the tests are shown in Fig. 30 as a load-COD diagram (average of 2-3 data for each alloy). Specimens of 9-Ni steel and Fe-Ni-Ti(1A) satisfied the ASTM thickness requirements for the plane strain condition. The fracture surfaces were completely flat with no shear lips as can be seen from the photograph of post-test fracture toughness specimens shown in Fig. 24(b). Plane-strain fracture toughness, K_{IC}, of 70-80 ksi $\sqrt{in.}$ was obtained for both 9-Ni steel and Fe-Ni-Ti(1A). Specimens of 304 stainless steel also showed flat fracture surface (Fig. 24(b)) but was not in the plane strain loading condition as can be seen from the extended load-COD curve in Fig. 30. The crack grew slowly and no "pop-in" occurred. Specimen 2B of Fe-Ni-Ti alloy (ultrafine grained) showed much higher load carrying capacity than any other specimens tested. The area under the load-COD curve was the largest among the specimens

tested at 6°K. The sudden drop of load in this specimen does not necessarily mean a fast crack propagation because slip (or yielding) near this temperature also occurs in a discontinuous manner (Fig. 13). Comparing the post-test specimens at 6°K shown in Fig. 24(b), the high toughness of this grain-refined specimen is visually apparent. Scanning electron fractographs were taken from the fracture surfaces of these 6°K specimens and are shown in Fig. 31. The quasi-cleavage fracture mode of 9-Ni steel and Fe-Ni-Ti(1A) is evident. 304 Stainless steel showed a peculiar fracture surface, which may be related to the TRIP phenomena near the crack tip. Fe-Ni-Ti(2B) showed essentially dimple rupture type fracture surface indicating ductile fracture mode. (Examination on the whole fracture surface except shear lip revealed that the fracture mode was a mixture of ~ 80% dimple rupture and ~ 20% quasi-cleavage.) Since a standardized method of fracture toughness evaluation for this type of load-COD curve at liquid helium temperature is not available, no fracture toughness measure was taken for this specimen other than a K_Q value.

VI. SUMMARY

(1) By alternate phase transformation in γ and $(\alpha+\gamma)$ range, the grain size of an Fe-12Ni-0.25Ti alloy was refined from 40-60 μm to 0.5-2 μm in 4 cycles.

(2) The yield strength of this thermally cycled alloy at 77°K and 4.2°K increased by 10-15 ksi, while the tensile ductility decreased slightly due to the grain refinement.

(3) No retained austenite was found before and after alternate thermal cycling, i.e. this alloy is completely ferritic unless additional treatment is added to introduced retained austenite.

(4) The lamellar type microstructure obtained after the first $(\alpha+\gamma)$ two phase range decomposition is detrimental to the cryogenic fracture toughness.

(5) With the ultrafine grain size obtained, the ductile-brittle transition temperature of this ferritic alloy in Charpy impact testing was suppressed below liquid helium temperature.

(6) The ductile-brittle transition temperature in a fracture toughness testing with a sharp crack was also suppressed below liquid helium temperature. At 77°K, fracture toughness (K_C) of roughly 470-500 ksi $\sqrt{\text{in.}}$ with yield strength of ~150 ksi was obtained with the grain refined Fe-12Ni-0.25Ti alloy. The fracture mode was also altered from brittle quasi-cleavage in a large grained alloy to completely ductile dimple rupture at 77°K and to essentially dimple type rupture at 6°K in a grain refined alloy.

(7) Additional treatment of 550°C/2 hours introduced 3-5% retained austenite which remained stable down to liquid nitrogen temperature. The effect of retained austenite was found to increase the shelf energy considerably in impact testing.

(8) Charpy impact tests obviously underestimate the ductile-brittle transition temperature.

(9) Compared to other commercial cryogenic alloys, grain-refined Fe-Ni-Ti alloy showed superior combination of strength and toughness down to liquid helium temperature.

ACKNOWLEDGEMENTS

The author wishes to express his deepest gratitude to Professor J. W. Morris, Jr. for his personal guidance, encouragement and support throughout the course of this research. He is also grateful to Professor V. F. Zackay for continuous advice and encouragement.

The assistance of the support staff of the Lawrence Berkeley Laboratory, Brian Pope (melting), Ed Edwards (specimen machining), John Holthuis (alloy preparation), Lee Johnson (metallography), George Georgakopoulos and George Gordon (scanning electron microscopy and X-ray analysis), Doug Kreitz (photography), Virgil Santos and Gary Gachis (cryogenic liquid), Sandy Stewart (purchasing), Gloria Pelatowski (drawing), and Alice Ramirez and Shirley Ashley (typing) is acknowledged. The author wishes to thank John Sanchez for his help in manuscript arrangement.

This work was supported by the Atomic Energy Commission through the Inorganic Materials Research Division of the Lawrence Berkeley Laboratory, and by the Office of Naval Research under contract N00014-69-A-1026, NR031-762.

REFERENCES

1. A. H. Cottrell, Trans. AIME 212, 192 (1958).
2. N. J. Petch, Phil. Mag. 3, 1089 (1958).
3. R. Armstrong, I. Codd, R. M. Douthwaite, and N. J. Petch, Phil. Mag. 7, 45 (1962).
4. N. S. Stoloff, "Fracture" edited by H. Liebowitz, Academic Press 6, 1 (1969).
5. N. S. Stoloff, "Proceedings of the Conference on Physical Basis of Yield and Fracture," Physical Society, London, p. 68 (1966).
6. J. M. Hodge, H. D. Manning, and H. M. Reichhold, Trans. AIME 185, 233 (1949).
7. M. Gensamer, Trans. AIME 215, 2 (1959).
8. G. Sasaki, (D. Eng. thesis) Univ. of Calif., Berkeley, 1973.
9. W. B. Morrison and W. C. Leslie, Met. Trans. 4, 379 (1973).
10. A. Crackwell and N. J. Petch, Acta Met. 3, 186 (1955).
11. W. C. Leslie, Met. Trans. 2, 1989 (1971).
12. W. C. Leslie, R. J. Sober, S. G. Babcock, and S. J. Green, Trans. ASM 62, 690 (1969).
13. I. Gupta, Met. Trans. 2, 323 (1971).
14. L. F. Porter and D. S. Dabkowski, "Ultrafine Grain Metals", Syracuse University Press, p. 113 (1972).
15. G. Saul, J. A. Roberson, and A. M. Adair, Met. Trans. 1, 383 (1970).
16. R. L. Miller, Met. Trans. 2, 905 (1972).
17. R. A. Grange, Trans. ASM, 59, 26 (1966).
18. S. Jin, J. W. Morris, Jr., and V. F. Zackay, Advances in Cryogenic Engineering, 19, 379 (1974).

19. S. Floreen, Met. Rev. p. 115 (1968).

20. M. Hansen, "Constitution of Binary Alloys", 2nd Ed., McGraw-Hill, New York, p. 677, 1958.

21. W. S. Owen, E. A. Wilson, and T. Bell, "High Strength Materials", edited by V. F. Zackay, John and Wiley, p. 167, 1965.

22. C. F. Hancock and G. M. Leak, Metal Sci. J. 1, 33 (1967).

23. R. L. Miller, Research Lab. of U.S. Steel Corp., Monroeville, Pennsylvania, Private Communication.

24. R. L. Miller, Trans. ASM 57, 892 (1964).

25. R. L. Miller, Trans. ASM 61, 592 (1968).

26. S. Floreen and G. R. Speich, Trans. ASM, 57, 714 (1964).

27. R. F. Decker, J. Metals, Nov., p. 60 (1967).

28. S. Floreen, Trans. ASM 57, 38 (1964).

29. T. Ooka, H. Mimura, S. Yano, K. Sugino and T. Toizumi, J. Japan Inst. Metals, 30, 442 (1966).

30. P. Legendre, Cobalt 29, 171 (1965).

31. G. T. Hahn and A. R. Rosenfield, ASTM STP 432, 1968.

32. D. T. Peters, Trans. ASM, 61, 62 (1968).

33. S. K. Hwang, S. Jin, and J. W. Morris, Jr., to be published.

34. E. B. Kula and T. S. DeSisto, "Behavior of Materials at Cryogenic Temperatures", ASTM STP 387, p. 1 (1965).

35. Z. S. Basinski, Proceedings Royal Society of London, 240, p. 229, (1957).

36. H. Conrad, "High Strength Materials", edited by V. F. Zackay, John and Wiley, p. 436 (1965).

37. 1973 Book of ASTM Standard, Part 31, E 23-72, p. 277.

38. S. Jin, W. A. Horwood, J. W. Morris, Jr., and V. F. Zackay, Advances in Cryogenic Engineering 19, 373 (1974).

39. T. S. DeSisto, Tech. Rep., 112/93, Watertown Arsenal Lab., July, 1958.

40. T. F. Keifer, Advances in Cryogenic Engineering 10, 56 (1965).

41. 1973 Book of ASTM Standard, Part 31, E 399-72, p. 960.

42. G. R. Irwin, "Structural Mechanics", Proceedings of the First Symposium on Naval Structural Mechanics, Pergamon Press, London, p. 557 (1960).

43. J. R. Rice, P. C. Paris, and J. G. Merkle, "Progress in Flow Growth and Fracture Toughness Testing", ASTM STP 536, p. 231 (1972).

44. J. A. Begley and J. D. Landes, "Fracture Toughness", ASTM STP 514, p. 1 (1972).

45. J. G. Merkle, "Progress in Flow Growth and Fracture Toughness Testing", ASTM STP 536, p. 264, (1972).

46. S. Jin, S. K. Hwang, and J. W. Morris, Jr., to be published.

Table I. Change of Phase Transformation Temperatures*

on Thermal Cycling (For 2 hours at Each Step)

	A_s	A_f	M_s	M_f
1A	673°C	715°C	473°C	412°C
IB	Isothermal		372°C	288°C
2A	642°C	726°C	473°C	367°C
2B	Isothermal		356°C	283°C

*Transformation temperatures were taken from the maxima or minima of the dilatometry curves. Measuring error of approximately ±3°C was noted.

Table II. Tensile Properties at 77°K

Alloy	Yield Strength* ksi	Tensile Strength ksi	Elong. %	R. A. %
Fe-Ni-Ti, 1A	134	142	31.1	73.8
1B	145	151	24.8	70.5
2A	141	150	29.3	72.9
2B	149	154	26.8	72.1
304 Stainless	81	235	47.3	65.6
9-Ni Steel	146	172	29.6	66.8

*0.2% offset yield strength

Table III. Tensile Properties at 4.2°K

Alloy	Yield Strength* ksi	Tensile Strength† ksi	Elong. %	R.A. %
Fe-Ni-Ti, 1A	182	207	23.8	72.9
2B	195	219	19.3	69.8
304 Stainless	105	270	41.6	52.7
9-Ni Steel	208	231	21.2	59.1

*Yield strength at 4.2°K was taken from the first discontinuous yield point.

†Tensile strength was obtained from the upper locus of discontinuous peaks in the stress-strain curve.

Table IV. Charpy Impact Testing at 77°K

	ASTM Standard Method	Proposed Method
Test Temperature	77°K	77°K
Method of Cooling	Open Air Transfer	Box System
Specimen Length	2.17 in. (55 mm)	2.01 in. (51 mm)
Number of Specimens Tested	17	17
Average Impact Energy	124.5 ft-lb (168.8 newton-m)	120.9 ft-lb (163.9 newton-m)
Standard Deviation	8.7 ft-lb (11.5 newton-m)	13.8 ft-lb (18.7 newton-m)

Table V. Charpy V-Notch Impact Energy at Cryogenic Temperatures

Alloy		Energy Absorbed (ft-lb)	
		77°K	6°K
Fe-12Ni-0.25Ti,	1A	154	55
	1B	116	43
	2A	131	116
	2B	115	99
304 Stainless		128	130
9-Ni Steel		92	75

Table VI. Fracture Toughness at Cryogenic Temperatures

	Alloy	Fracture Toughness ksi $\sqrt{in.}$	Remarks
77°K	Fe-12Ni-0.25Ti, 1A	K_Q = 130-150	ASTM
	1B	K_Q = 90-110	ASTM
	2A	K_Q = 130-150	ASTM
	2B	K_Q = 130-150	ASTM
		K_C = 470-500	Based on Work of Fracture
	304 Stainless	K_Q = 60-70	ASTM
		K_C = 350-380	Based on Work of Fracture
	9-Ni Steel	K_Q = 120-140	ASTM
6°K	Fe-12Ni-0.25Ti, 1A	K_{IC} = 70-80	ASTM (plane strain)
	2B	K_Q = 150-170	ASTM
		K_C = ?	not evaluated
	304 stainless	K_Q = 80-100	ASTM
		K_C = 280-300	Based on Work of Fracture
	9-Ni steel	K_{IC} = 70-80	ASTM (plane strain)

FIGURE CAPTIONS

Fig. 1. The Fe-Ni equilibrium phase diagram with heat treating cycles.

Fig. 2. Transmission electron micrographs of the Fe-12Ni-0.25Ti alloy. The specimen was annealed at 900°C for 2 hours and 730°C for 2 hours.

Fig. 3. Another area of the same specimen shown in Fig. 2.

Fig. 4. Dilatometric analysis of the phase transformations in Fe-12Ni-0.25Ti alloy, (a) on continuous heating and cooling, (b) on isothermal decompositionwithin the($\alpha+\gamma$) range for different periods.

Fig. 5. Estimated isothermal transformation rate at 650°C.

Fig. 6. (a) Dilatometry for an initially homogeneous specimen (same as Fig. 4(a), (b) dilatometry for a specimen initially decomposed at 650°C for 2 hours. After the transformation of the duplex structure to γ is finished, the specimen was held at 730°C for two hours for partial homogenization and then cooled to room temperature, (c) same as (b) except that the homogenization was minimized by holding at 730°C for just a few seconds. (d) The homogenization cycle (b) was followed by another continuous heating to the γ range to see the change in A_s, A_f temperatures from those of (a) and (b).

Fig. 7. Change of optical microstructures on thermal cyclings. (a) starting microstructure (900°C 2 hours annealed), (b) after cycle 1A, (c) after cycle 1B, (d) after cycle 2A, (e) after cycle 2B (final microstructure).

Fig. 8. Scanning electron microstructures. (a) specimen 1B. (b) specimen 2A, (c) specimen 2B.

Fig. 9. Dilatometric analysis of the isothermal decomposition within the ($\alpha+\gamma$) two phase range at different temperatures. Subsequent phase transformations are also shown.

Fig. 10. Transmission electron micrograph of the specimen grain refined and annealed at 550°C for 2 hours. Selected area diffraction pattern is also shown.

Fig. 11. Diffraction pattern, bright field electron micrograph are shown together with a corresponding dark field photograph taken from $(200)_\gamma$ spot. Retained austenite is shown in the dark field.

Fig. 12. Diffraction pattern, bright field and dark field electron micrographs showing the location of retained austenite.

Fig. 13. Engineering stress-strain curves obtained in the tensile tests at 77°K and 4.2°K.

Fig. 14. Grooves made on each piece of the styrofoam layer. (Grooved side is to face the metal specimen.)

Fig. 15. Specimen packing inside a lucite box (top view).

Fig. 16. Schematic illustration of the test method (front view).

Fig. 17. Transfer of liquid helium to the box system. (Liquid helium is about to come out.)

Fig. 18. Cooling curves obtained using Au(0.07% Fe)--chromel thermocouple.
a. Thermocouple tip is directly immensed in liquid helium.
b. Specimen temperature when liquid helium is transferred.

Fig. 19. Photographs of the broken Charpy bars of the Fe-12Ni-0.25Ti alloy after testing at 77°K and 6°K.

Fig. 20. Load-crack opening displacement curves in fracture toughness testing at 77°K.

Fig. 21. Post-test fracture toughness specimens.

Fig. 22. Scanning electron microscope fractographs of the specimens shown in Fig. 21.

Fig. 23. Comparison of Load-COD curves of the Fe-12Ni-0.25Ti alloys, commercial 9-Ni steel and 304 stainless steel at 77°K.

Fig. 24. Comparison of the fracture toughness specimens tested at (a) 77°K and (b) 6°K.

Fig. 25. Lucite box system to encase the fracture toughness specimen and the styrofoam during the fracture toughness testing at liquid helium temperature. Holes in the lucite box were made elongated to prevent cracking of the box when the specimen was pulled.

Fig. 26. Front view (schematic) of the box system placed into the MTS machine. A 1/16 in. diameter hole was drilled near the crack tip down to the center line of specimen thickness. A plastic tubing was glued onto this hole. This tube sticks out through the hole in the lucite box, and the thermocouple is placed through the tube.

Fig. 27. Side view (schematic) of the box system.

Fig. 28. Photographs showing the fracture toughness test procedure at 6°K. (a) Box system is placed into the MTS testing machine. A strain-gauge, a thermocouple and a liquid helium transfer line are also in place. A thin sheet of Myler was used to

protect the strain gauge from liquid helium. (b) Transfer of liquid helium is initiated. (c) When the specimen was cooled down to ~ 6°K, the test was started. Air gun helps removing helium vapor from the vicinity of the strain gauge. (d) Specimen was broken and the test was finished. Lucite box remained safe without cracking.

Fig. 29. Change of specimen temperature during the test is shown as a function of time. Liquid helium transfer was initiated at t=0.

Fig. 30. Load-COD curves in fracture toughness testing at 6°K.

Fig. 31. Scanning electron microscopy fractographs of the fracture toughness specimens tested at 6°K (Fig. 24(b).

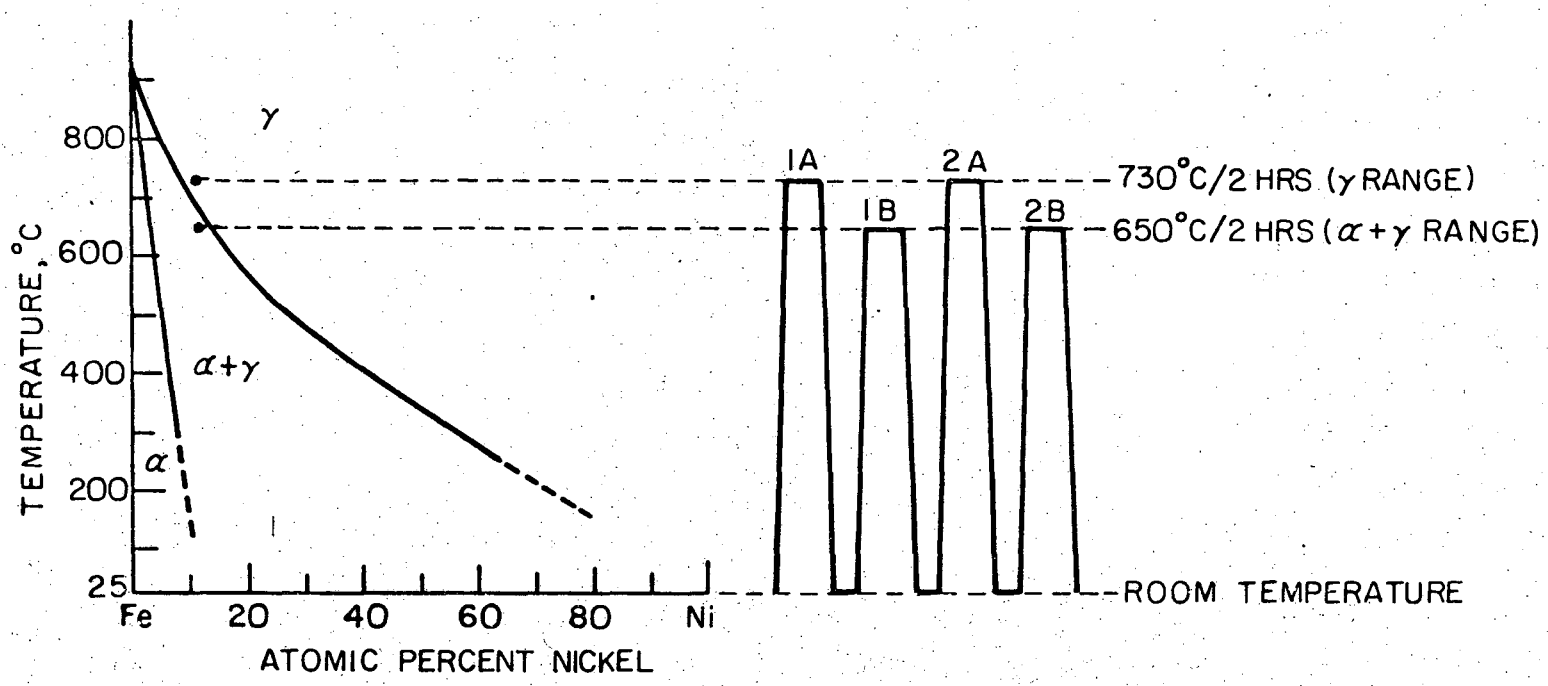

XBL 739-1884

Fig. 1.

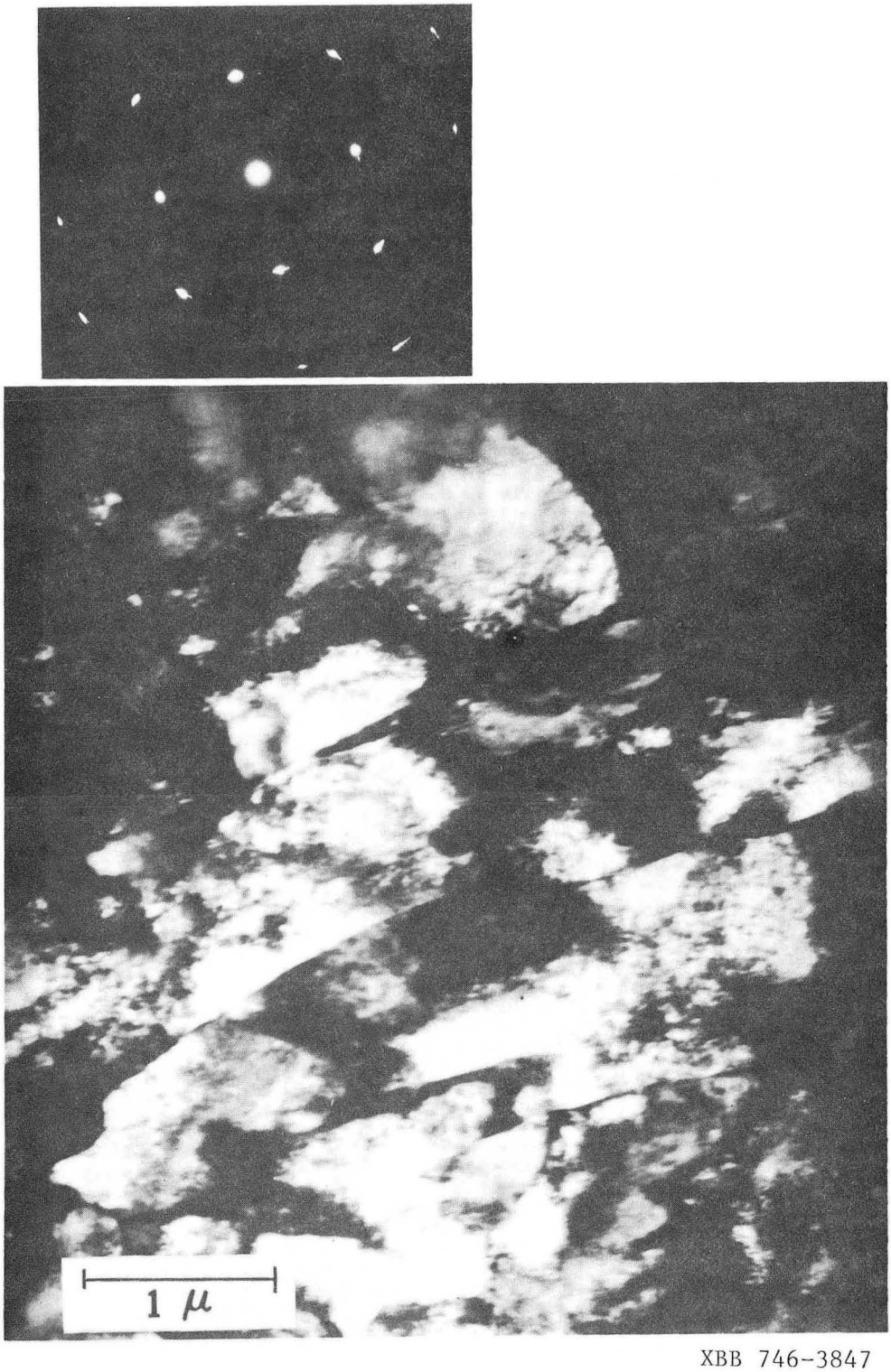

XBB 746-3847

Fig. 2.

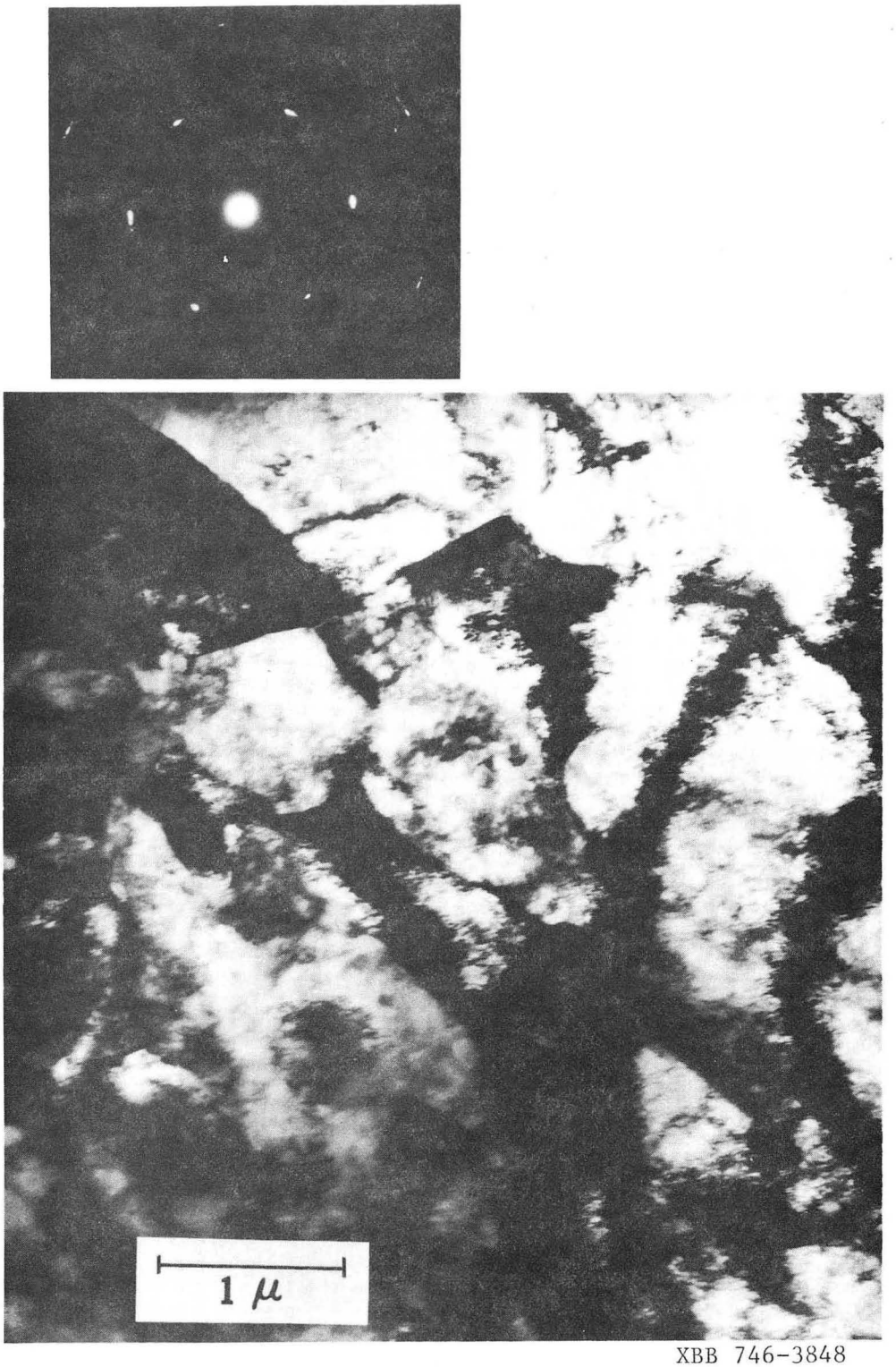

XBB 746-3848

Fig. 3.

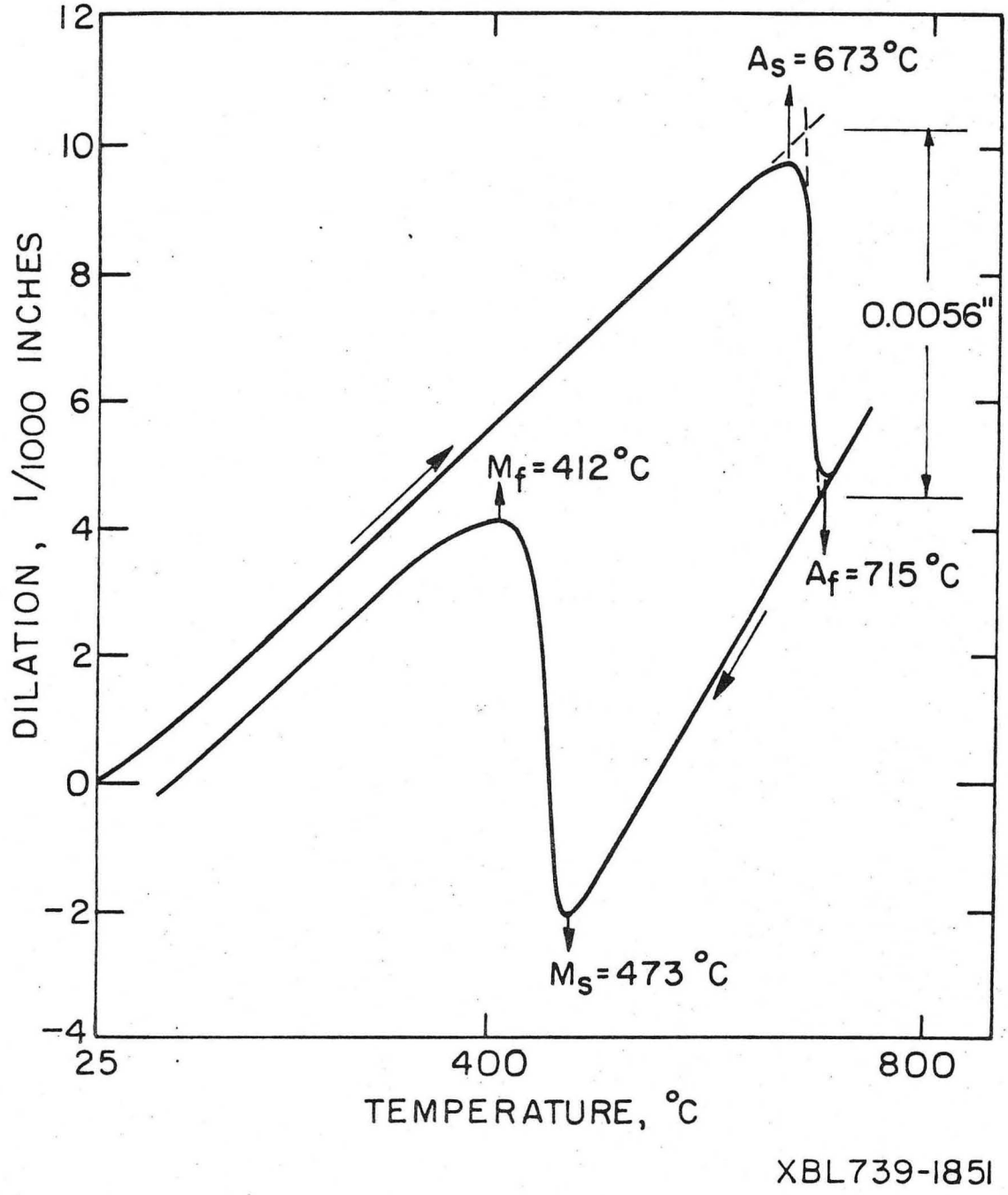
12
10
8
6
4
2
0
-2
-4
DILATION, 1/1000 INCHES
25
400
800
TEMPERATURE, °C
A_s = 673°C
M_f = 412°C
A_f = 715°C
M_s = 473°C
0.0056"
XBL739-1851

Fig. 4(a).

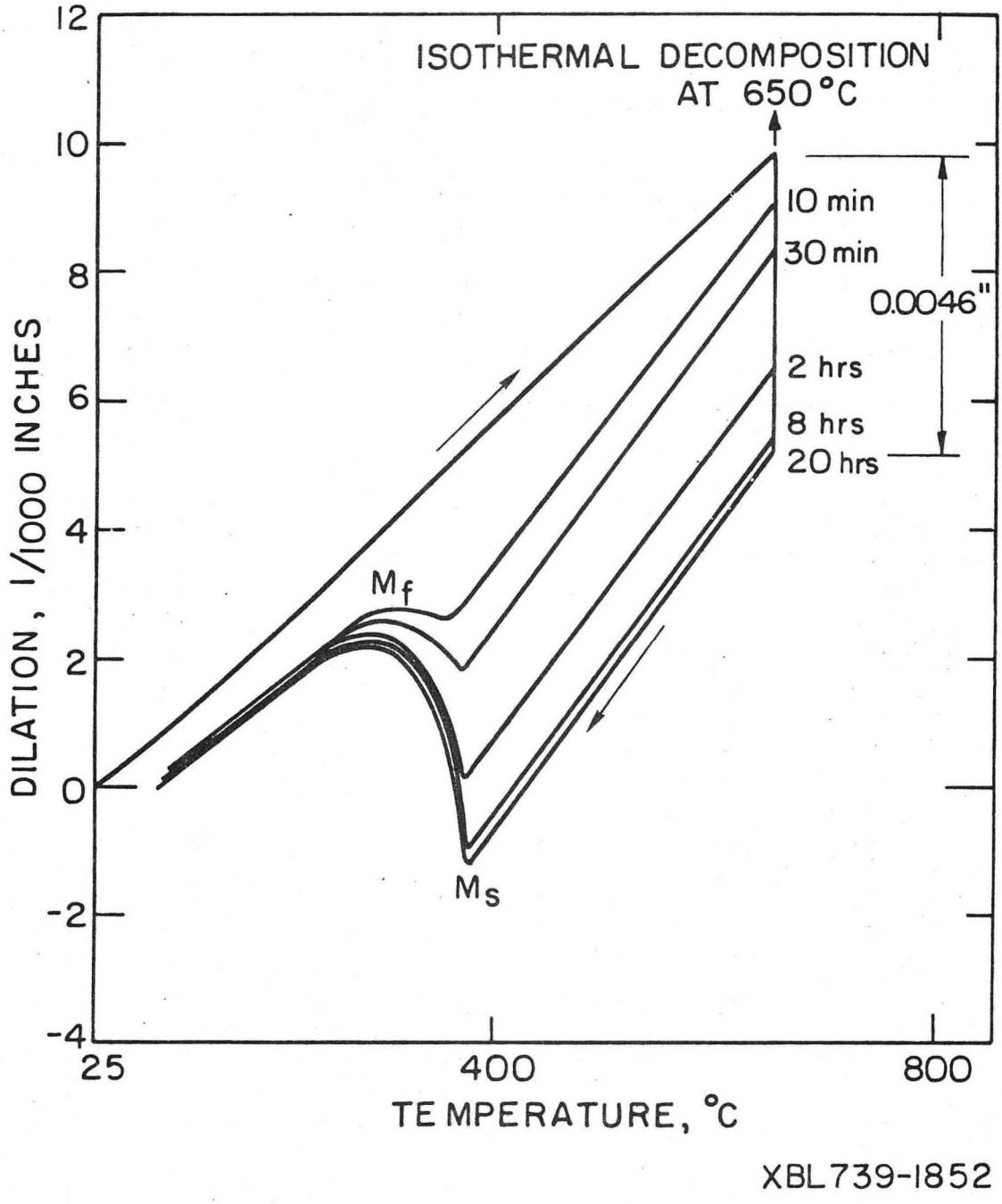
ISOTHERMAL DECOMPOSITION
AT 650°C
10 min
30 min
0.0046"
2 hrs
8 hrs
20 hrs
M_f
M_s
DILATION, 1/1000 INCHES
TEMPERATURE, °C
12
10
8
6
4
2
0
-2
-4
25
400
800
XBL739-1852

Fig. 4(b).

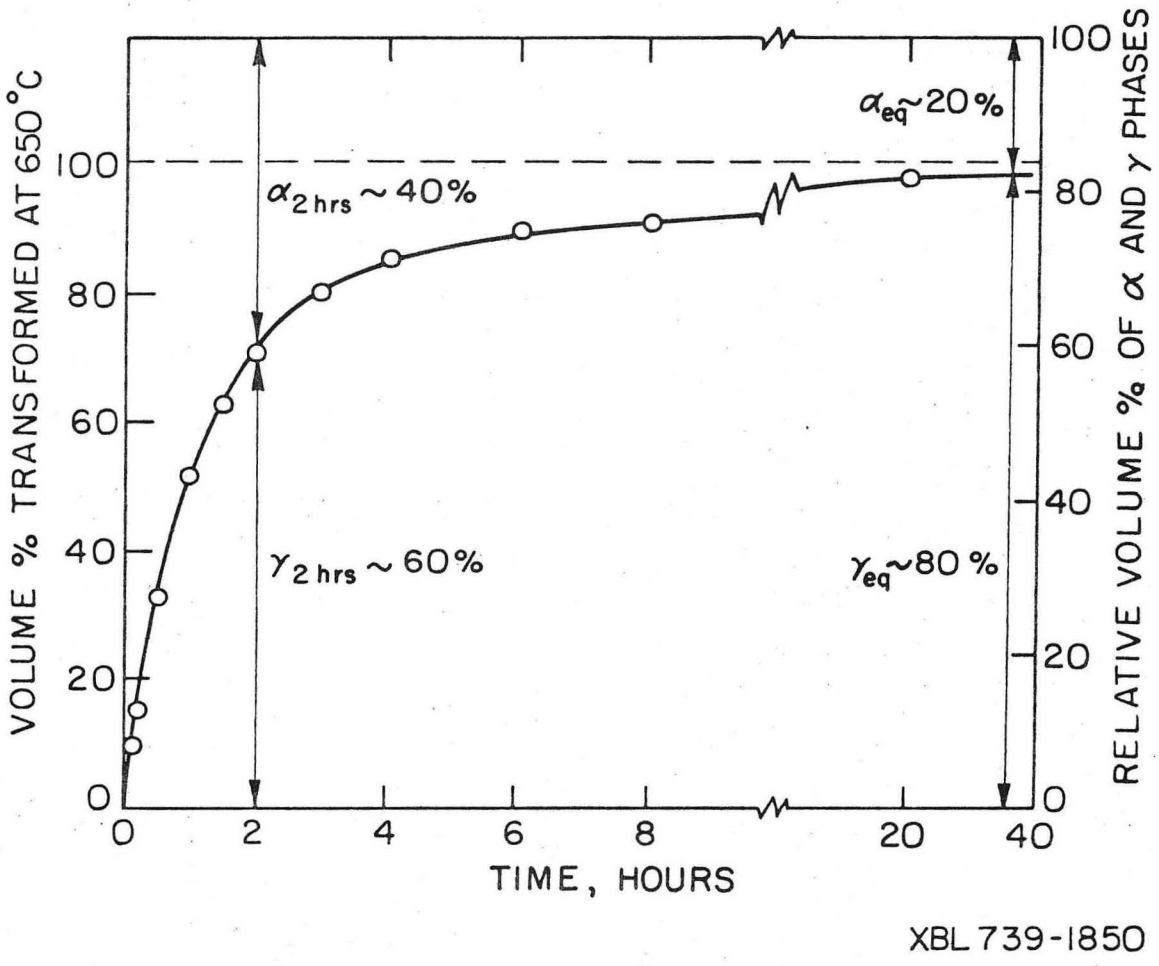
VOLUME % TRANSFORMED AT 650°C
RELATIVE VOLUME % OF α AND γ PHASES
TIME, HOURS
$\alpha_{2\,hrs} \sim 40\%$
$\gamma_{2\,hrs} \sim 60\%$
$\alpha_{eq} \sim 20\%$
$\gamma_{eq} \sim 80\%$
0
20
40
60
80
100
0
2
4
6
8
20
40
XBL 739-1850

Fig. 5.

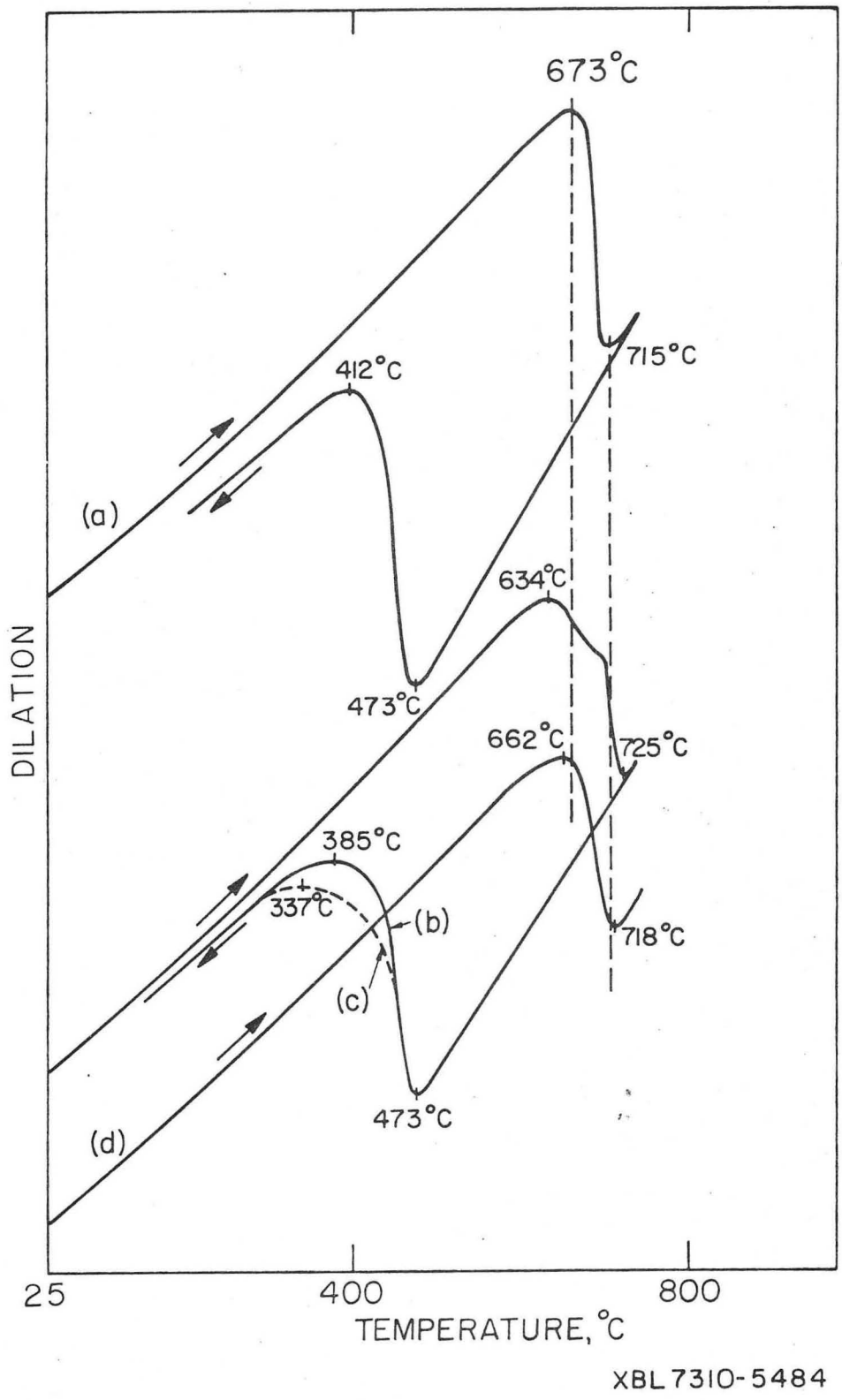
673°C
412°C
715°C
(a)
634°C
473°C
662°C
725°C
385°C
337°C
(b)
718°C
(c)
473°C
(d)
DILATION
25
400
800
TEMPERATURE, °C
XBL 7310-5484

Fig. 6.

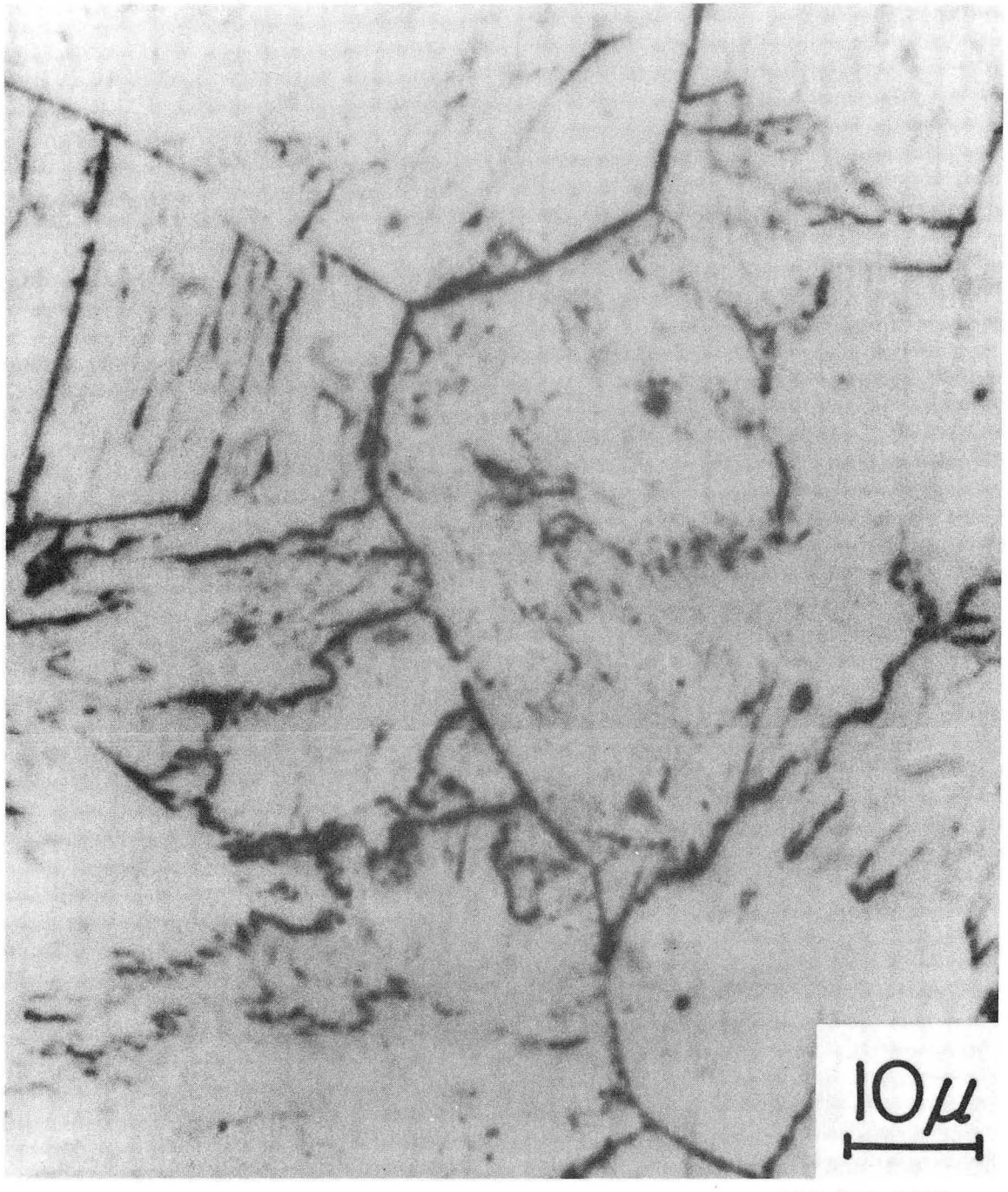

XBB 739-5688

Fig. 7(a).

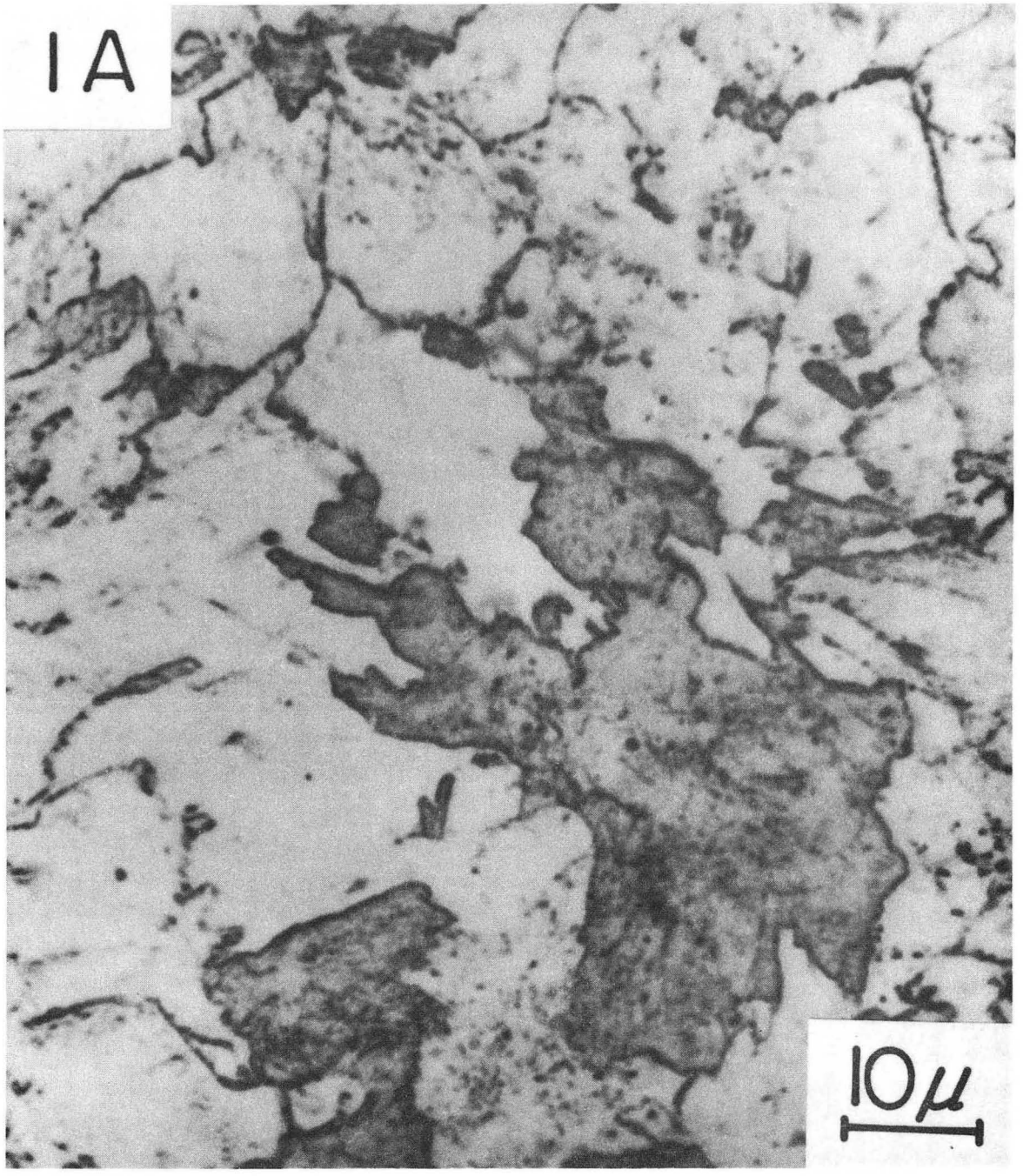

XBB 739-5689

Fig. 7(b).

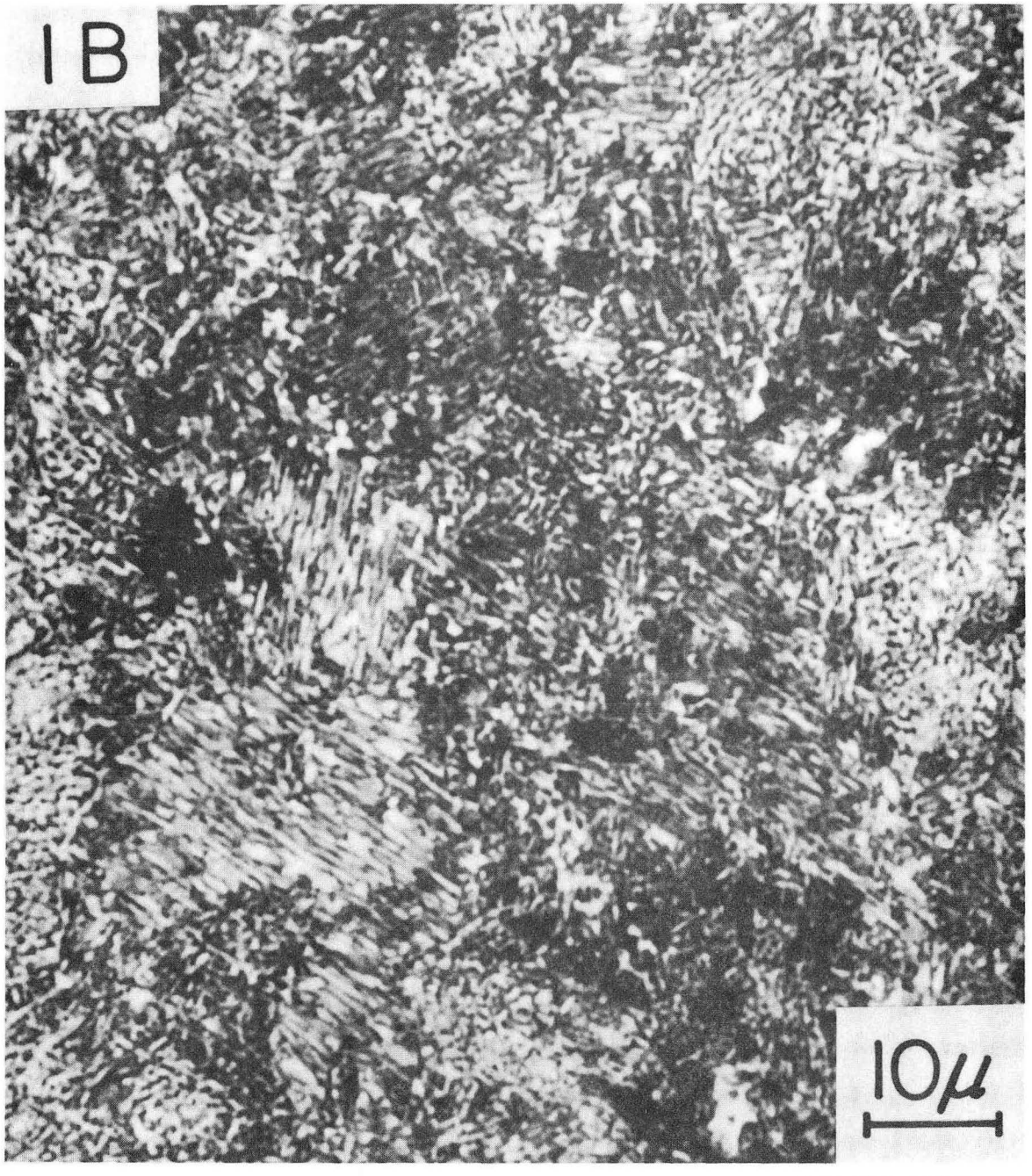

XBB 739-5690

Fig. 7(c).

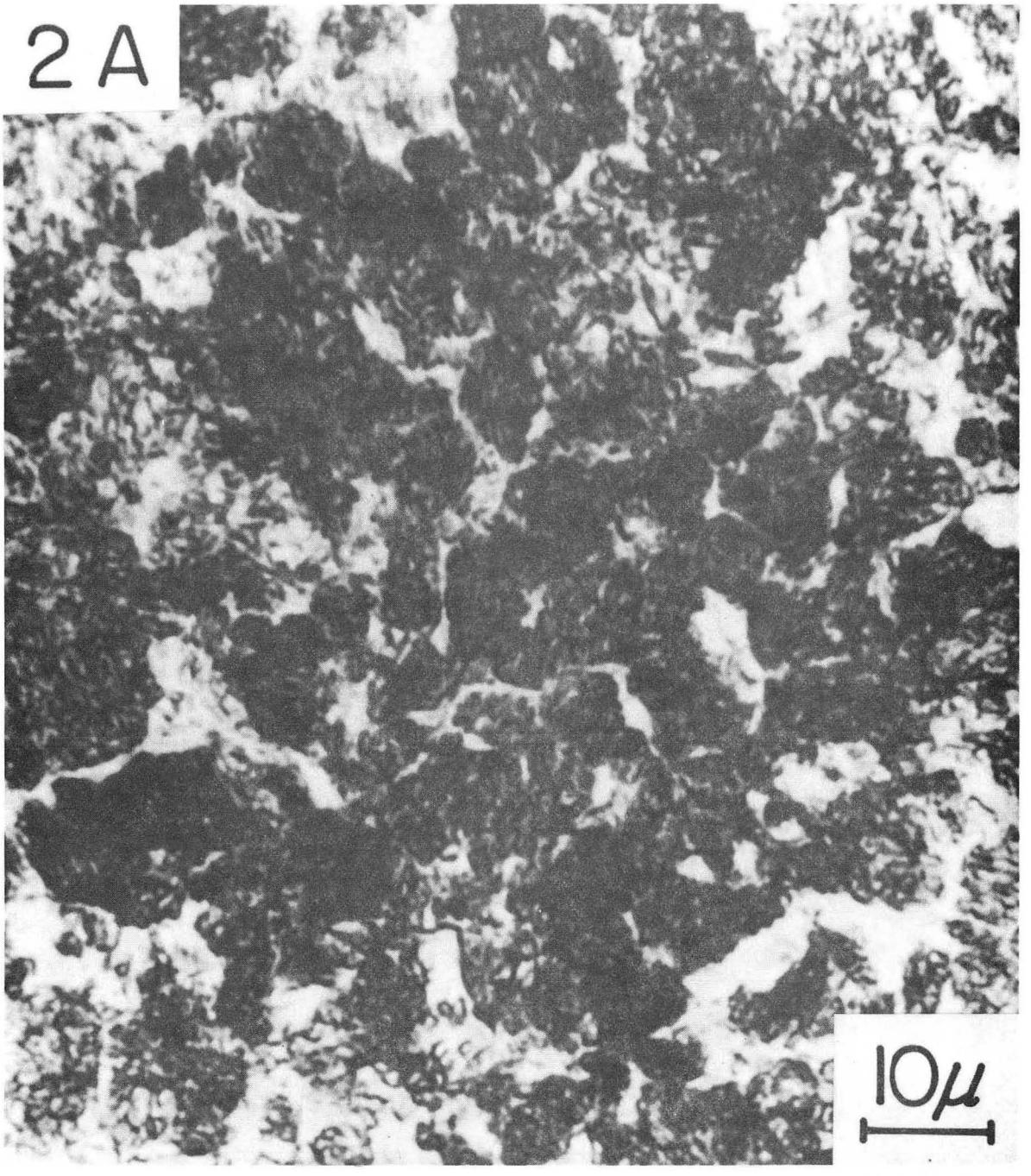

XBB 739-5691

Fig. 7(d).

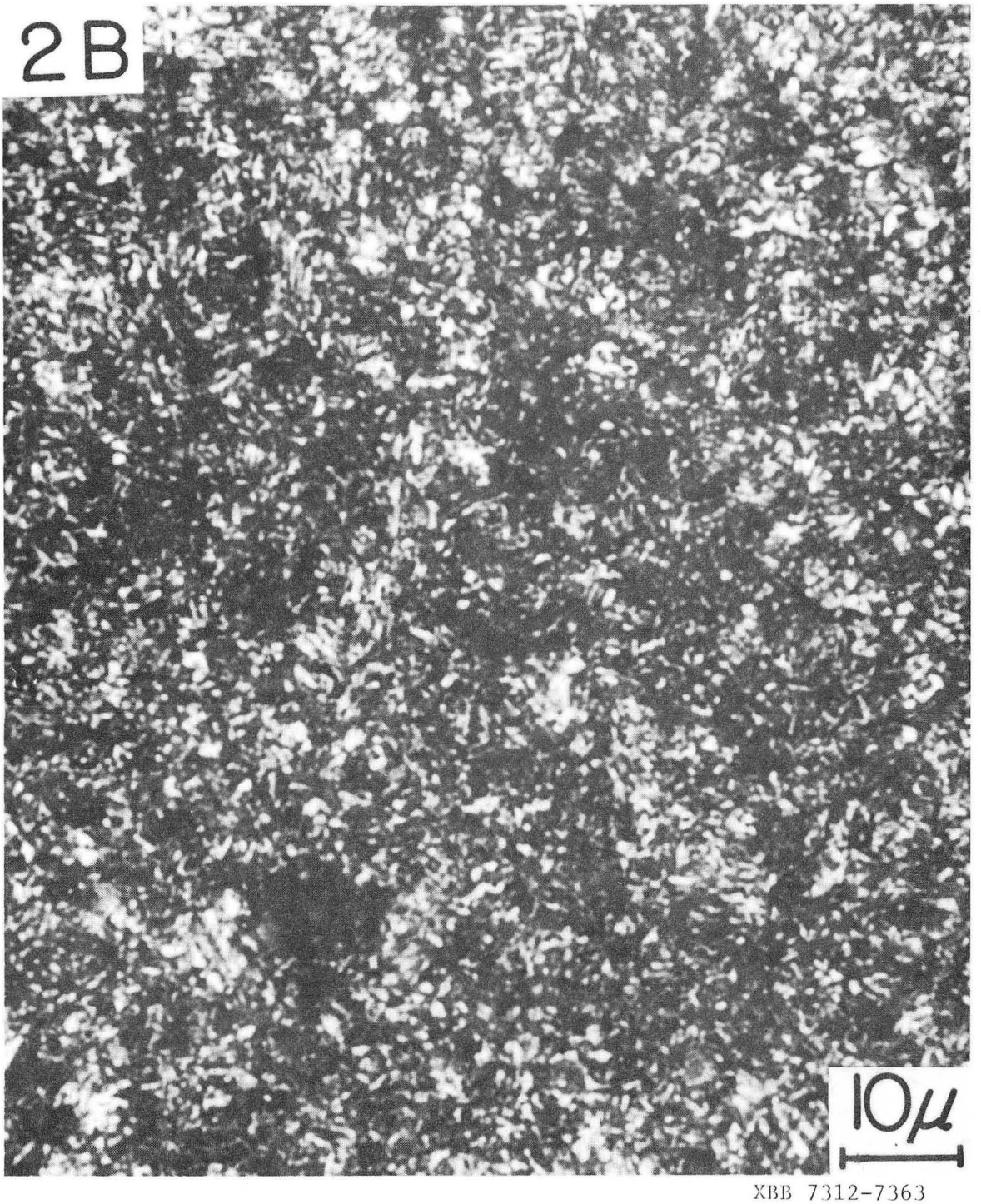

XBB 7312-7363

Fig. 7(c).

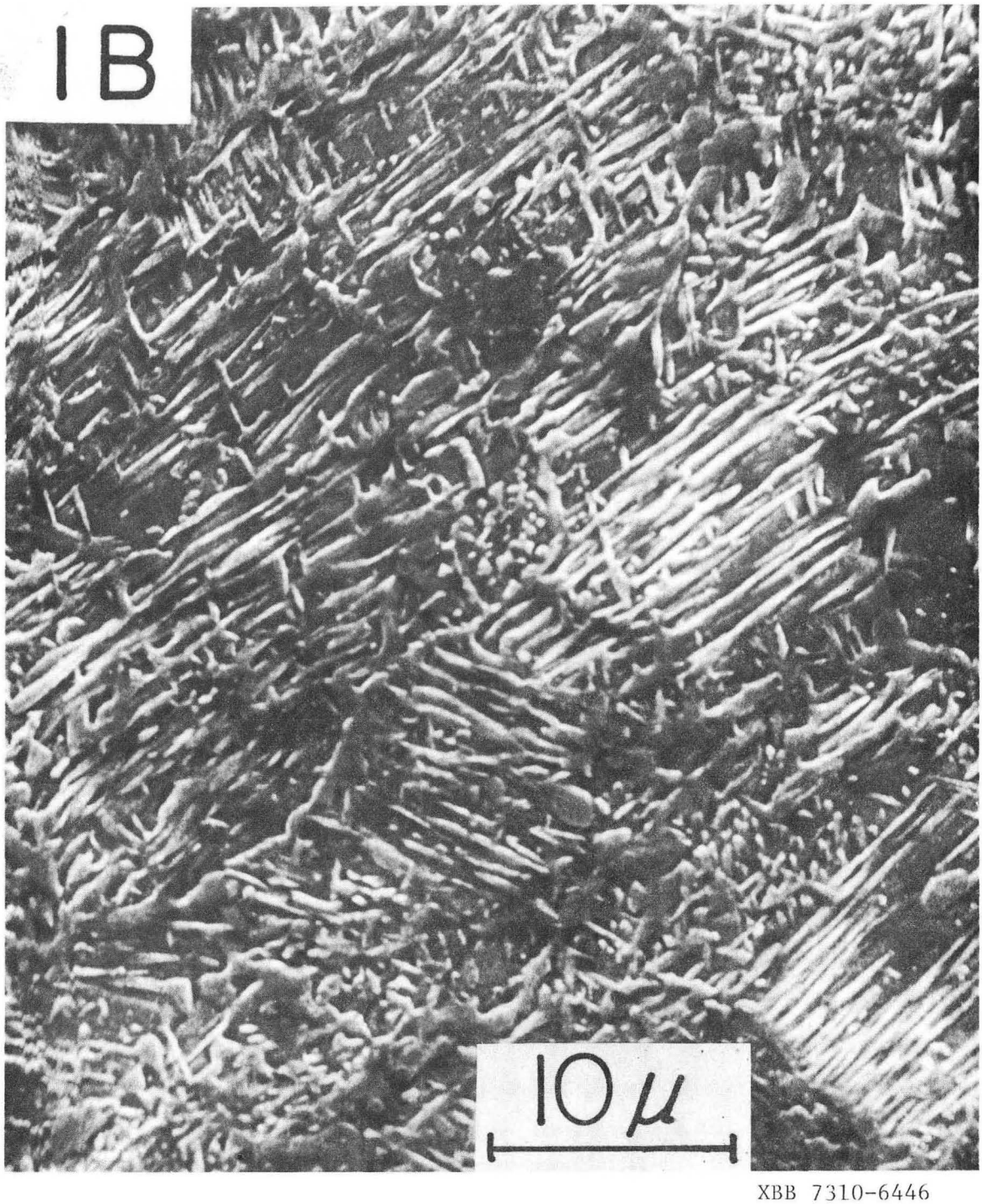

XBB 7310-6446

Fig. 8(a).

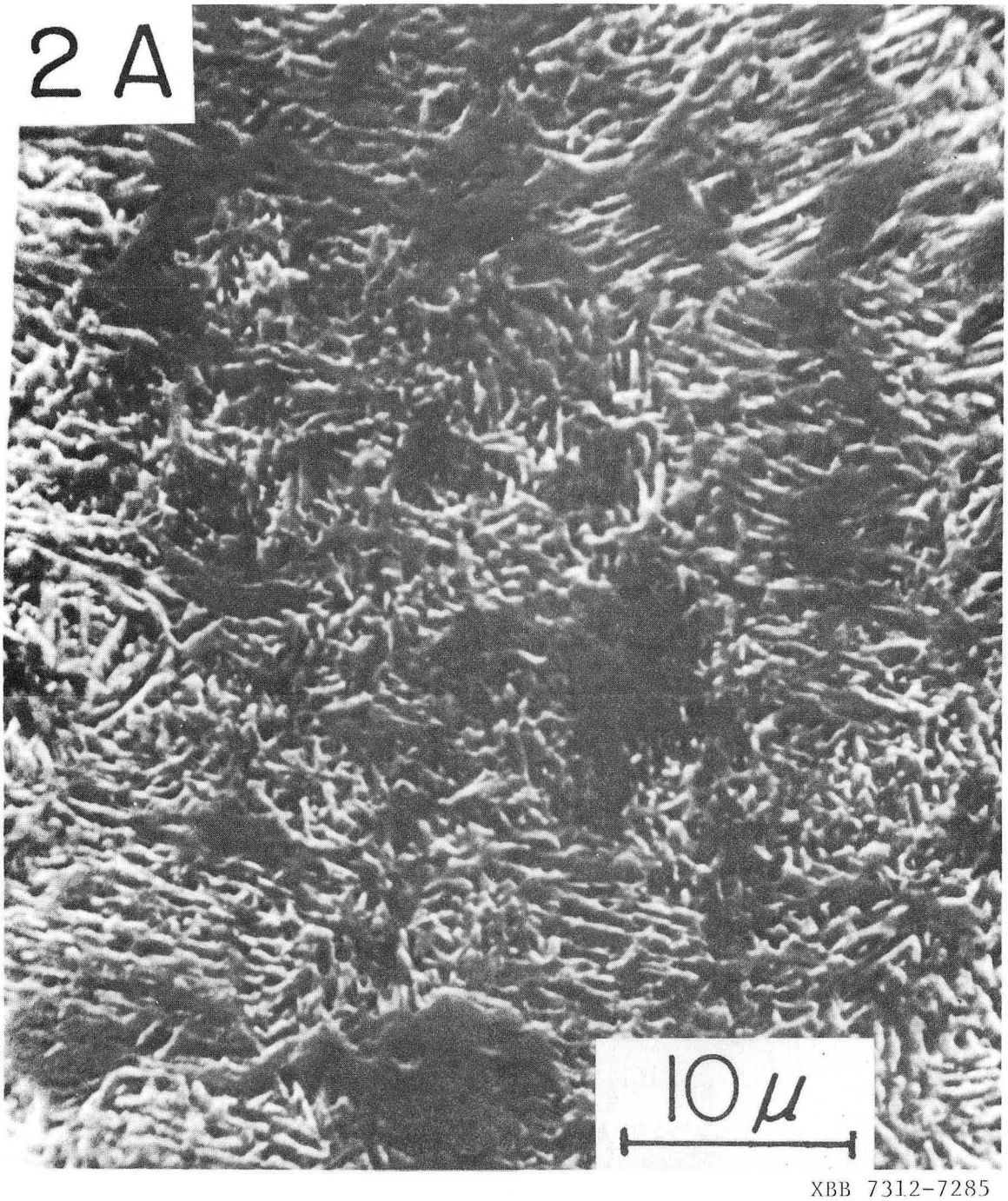

XBB 7312-7285

Fig. 8(b).

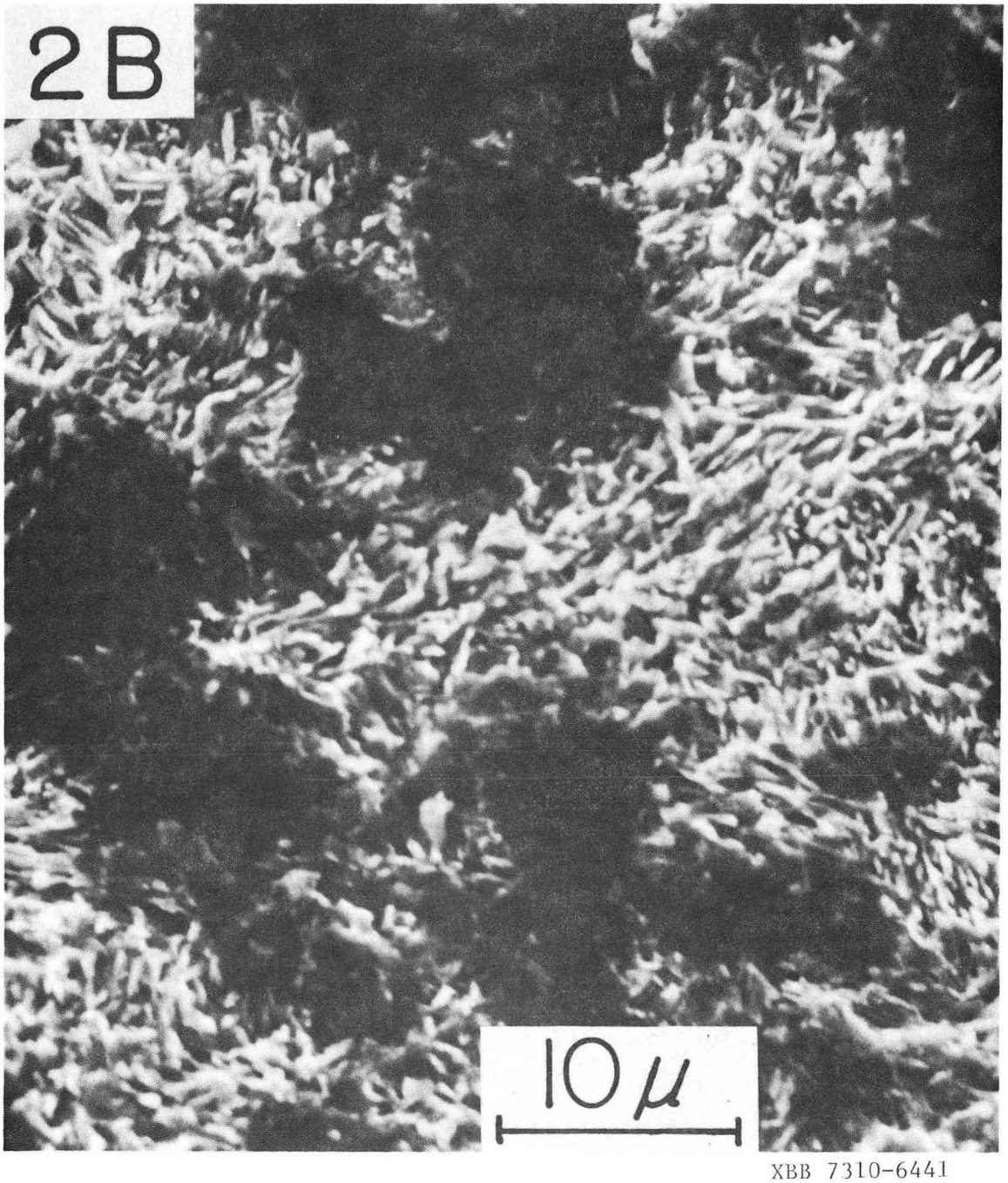

XBB 7310-6441

Fig. 8(c).

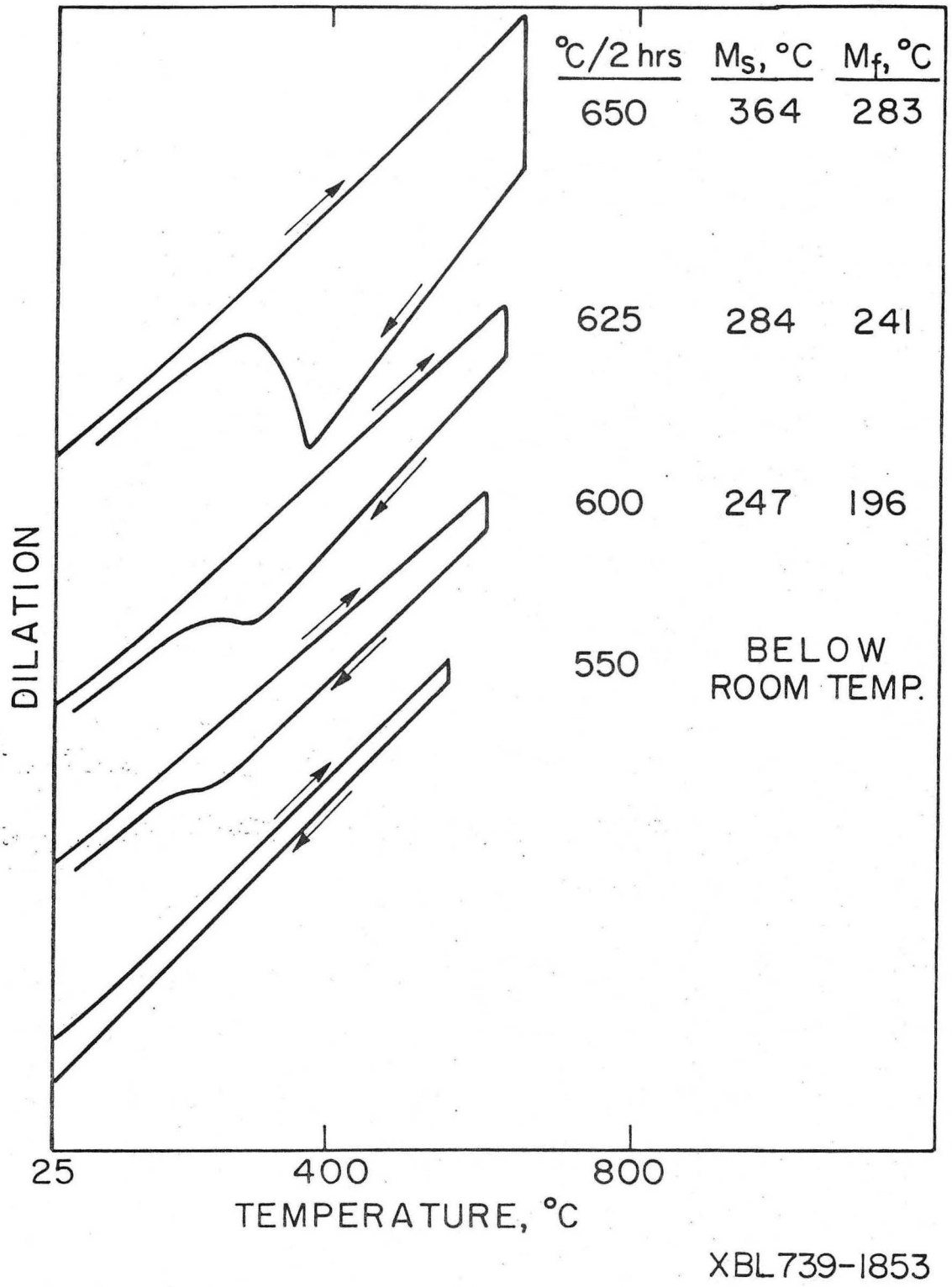
°C/2 hrs
Ms, °C
Mf, °C
650
364
283
625
284
241
600
247
196
550
BELOW
ROOM TEMP.
DILATION
25
400
800
TEMPERATURE, °C
XBL739-1853

Fig. 9.

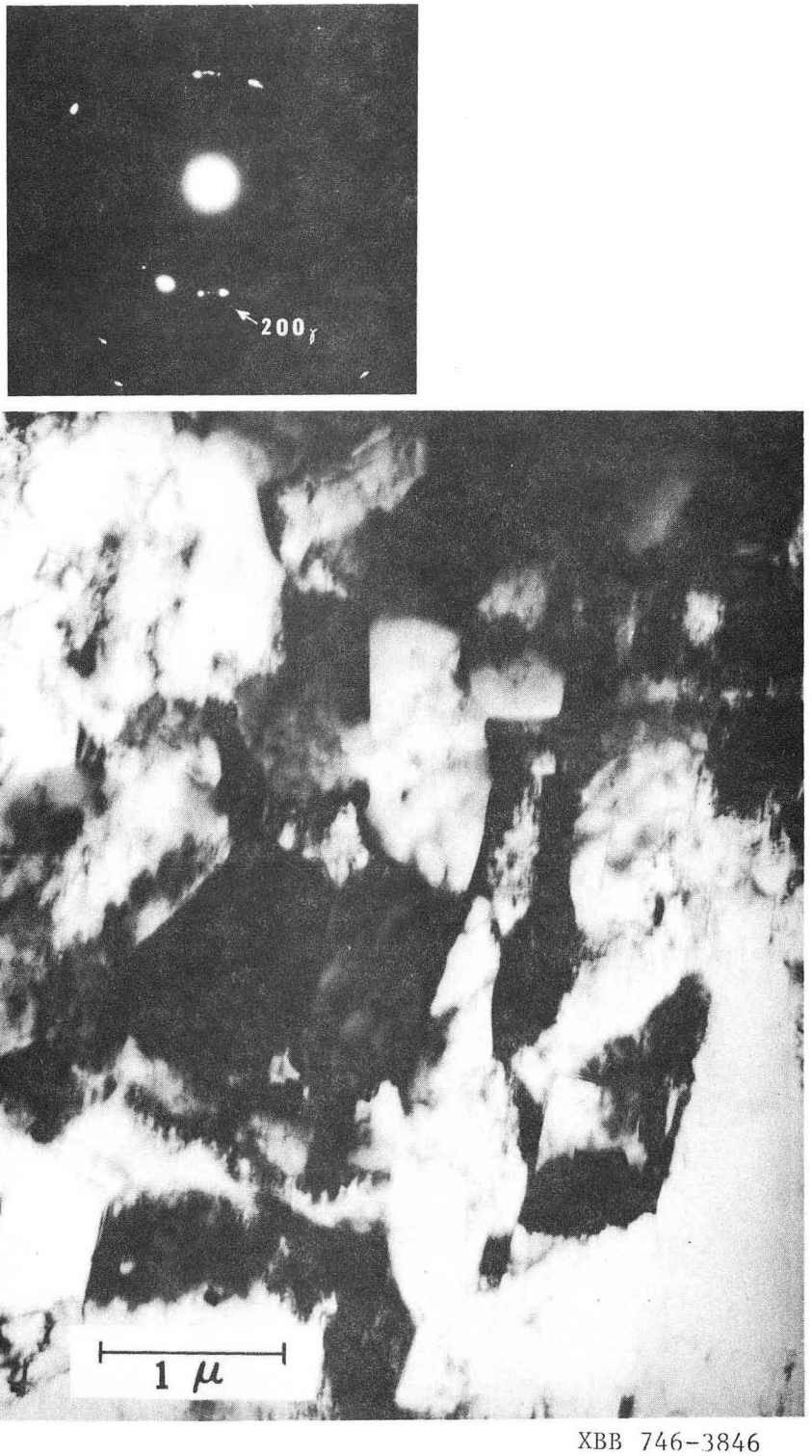

XBB 746-3846

Fig. 10.

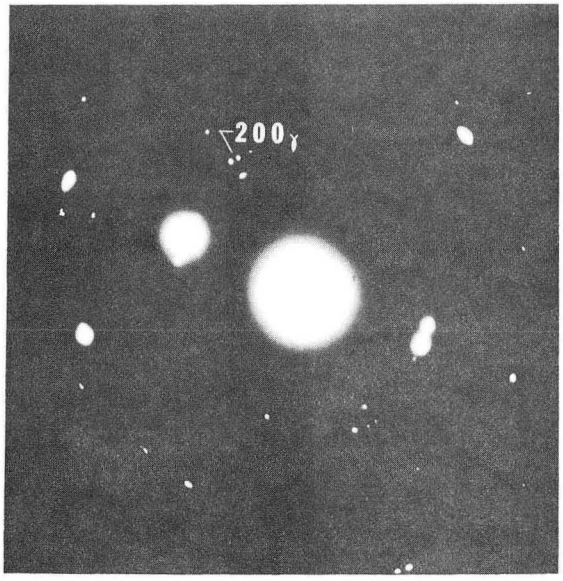

SAD

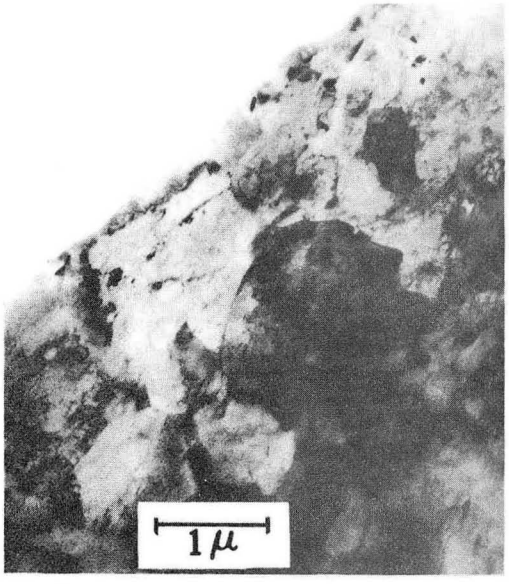

BF

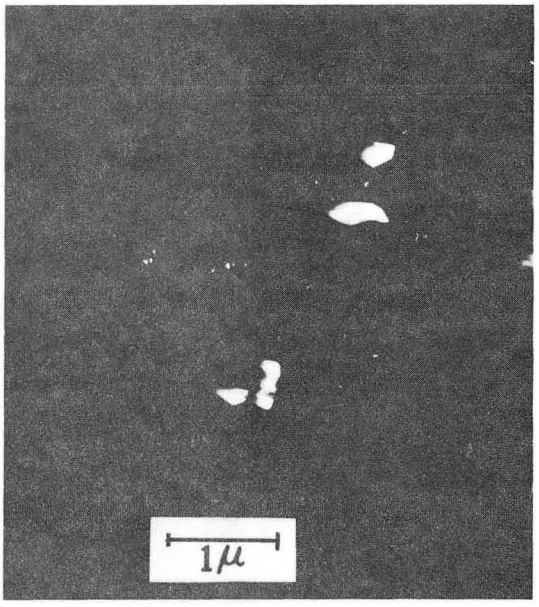

DF

XBB 746-3850

Fig. 11.

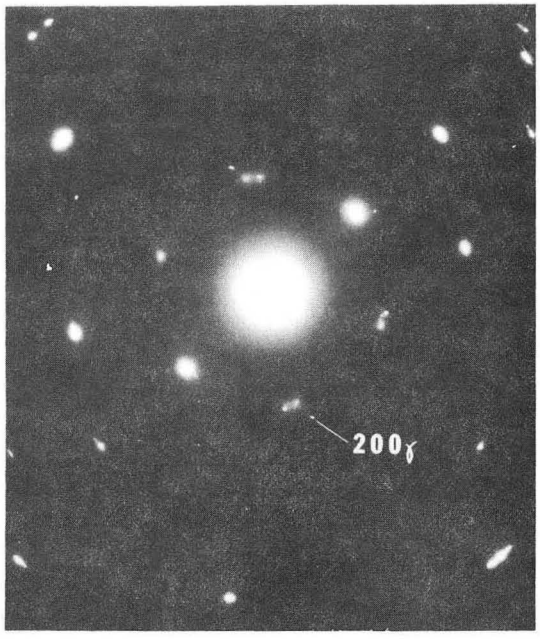

SAD

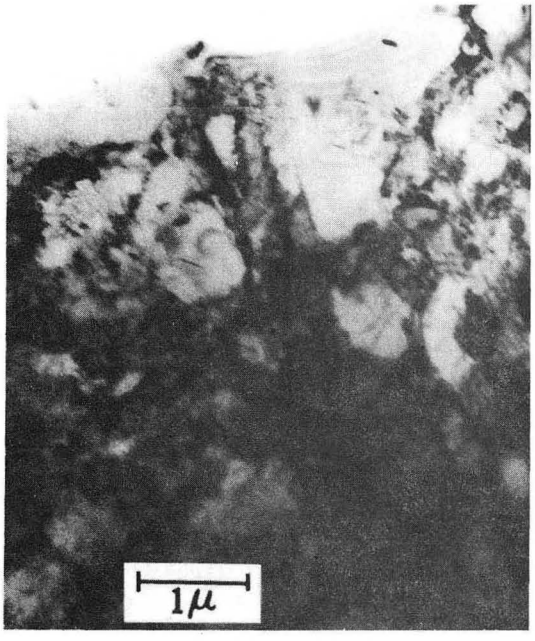

BF

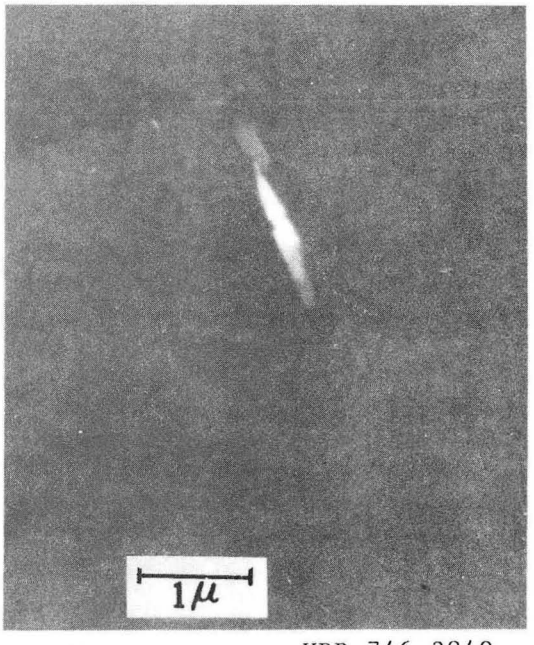

DF

XBB 746-3849

Fig. 12.

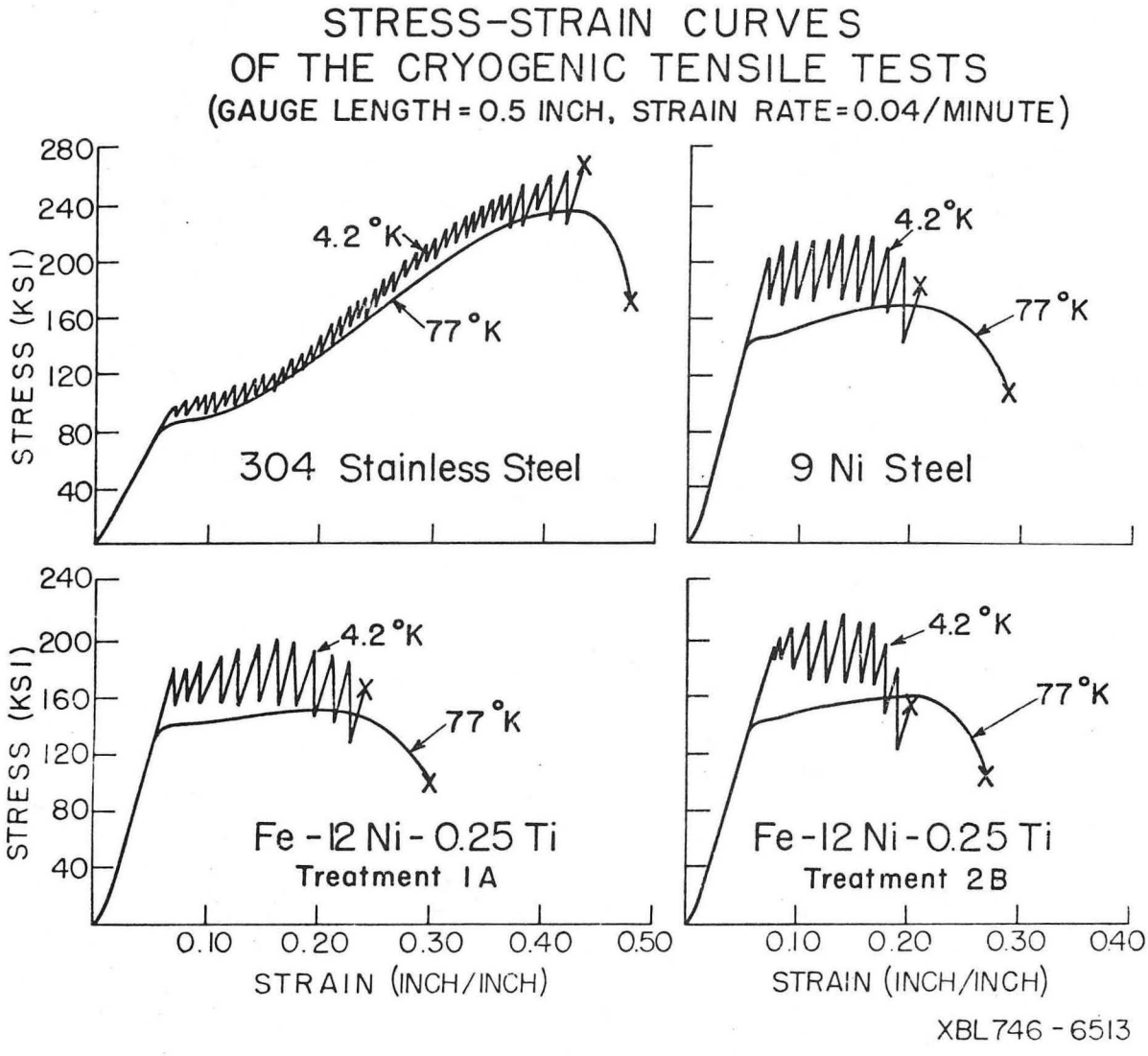
STRESS-STRAIN CURVES
OF THE CRYOGENIC TENSILE TESTS
(GAUGE LENGTH = 0.5 INCH, STRAIN RATE = 0.04/MINUTE)
STRESS (KSI)
280
240
200
160
120
80
40
4.2 °K
77 °K
304 Stainless Steel
9 Ni Steel
Fe - 12 Ni - 0.25 Ti
Treatment 1A
Fe - 12 Ni - 0.25 Ti
Treatment 2B
0.10
0.20
0.30
0.40
0.50
STRAIN (INCH/INCH)
XBL746 - 6513

Fig. 13.

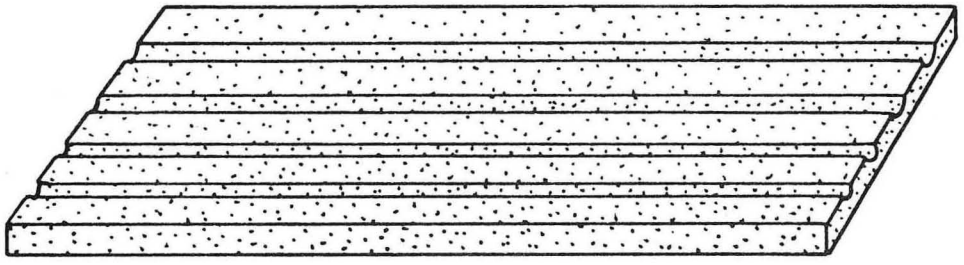

XBL 732-5792

Fig. 14.

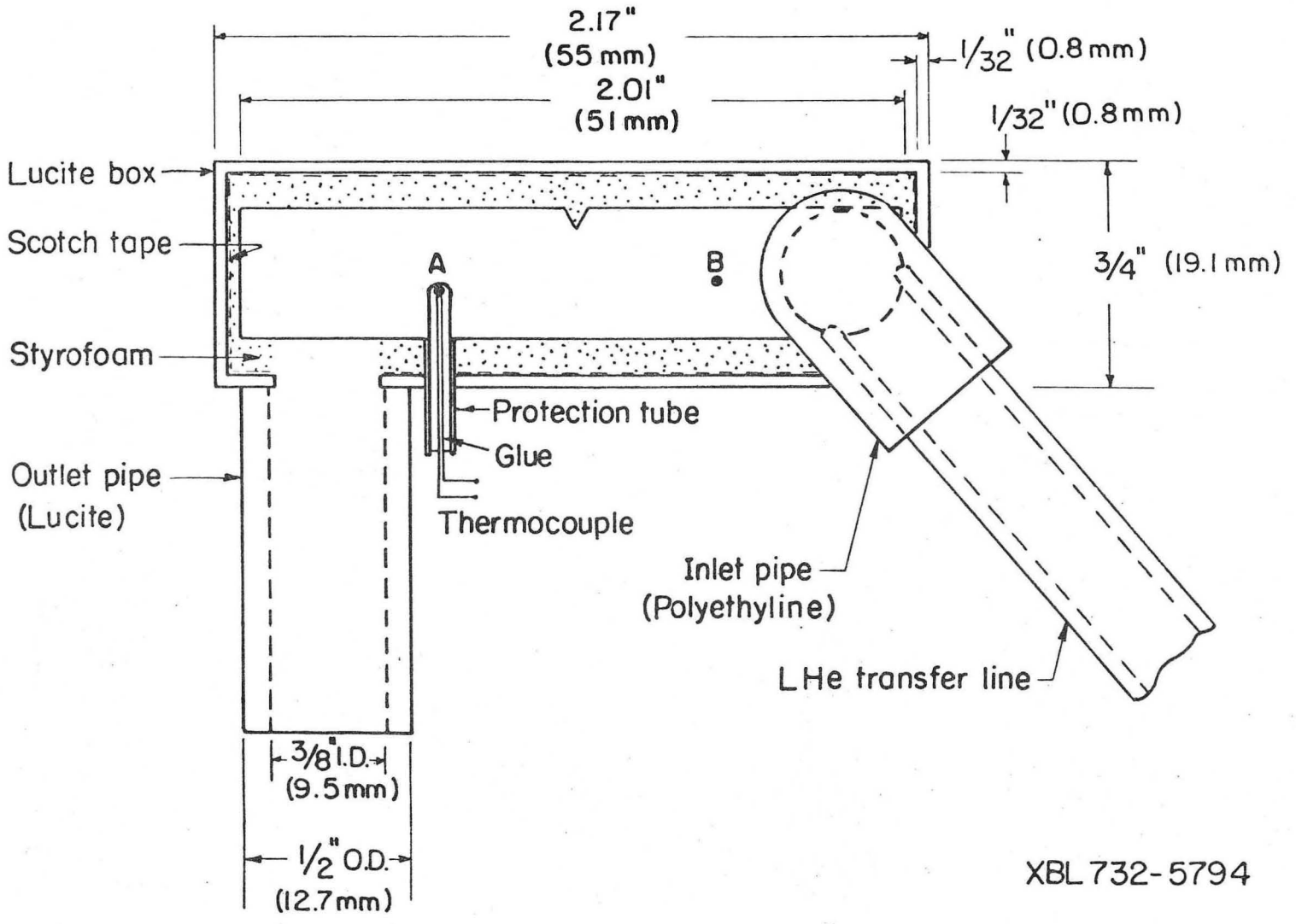
2.17"
(55 mm)
2.01"
(51 mm)
1/32" (0.8 mm)
1/32" (0.8 mm)
3/4" (19.1 mm)
Lucite box
Scotch tape
Styrofoam
Outlet pipe
(Lucite)
A
B
Protection tube
Glue
Thermocouple
Inlet pipe
(Polyethyline)
LHe transfer line
3/8" I.D.
(9.5 mm)
1/2" O.D.
(12.7 mm)
XBL 732-5794

Fig. 15.

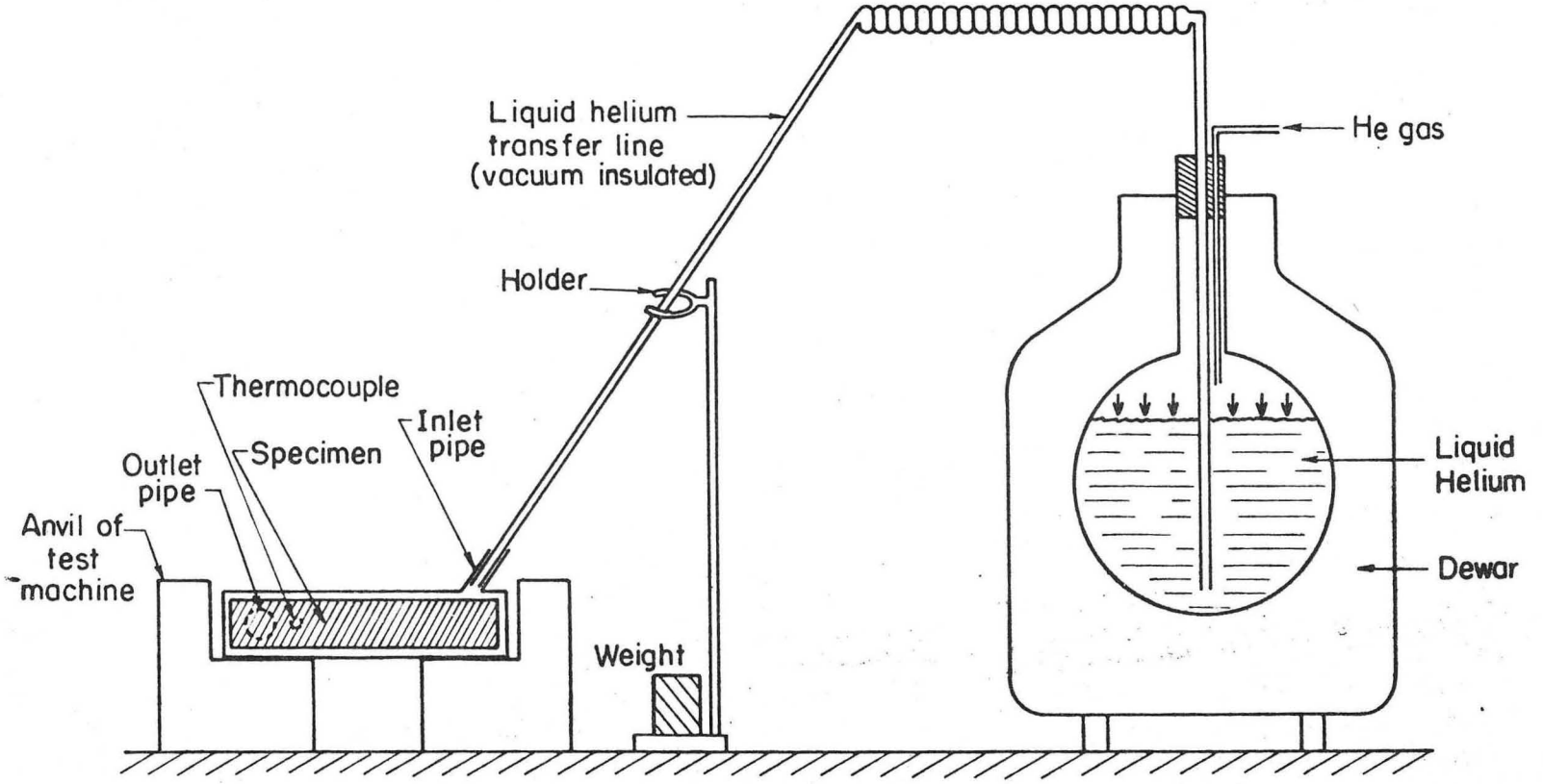
Liquid helium
transfer line
(vacuum insulated)
He gas
Holder
Thermocouple
Inlet
pipe
Specimen
Outlet
pipe
Anvil of
test
machine
Liquid
Helium
Dewar
Weight
XBL 732-5793

Fig. 16.

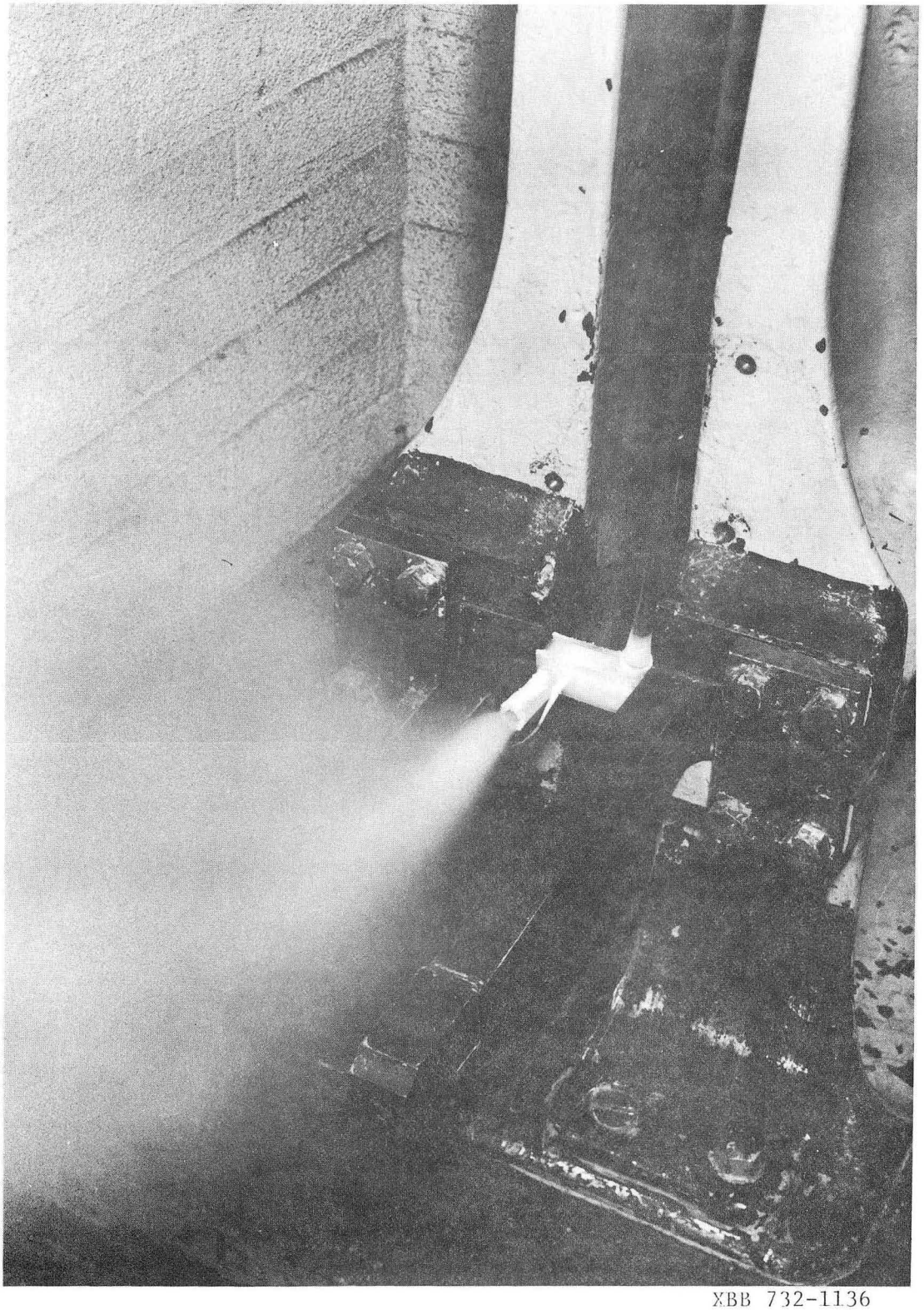

XBB 732-1136

Fig. 17.

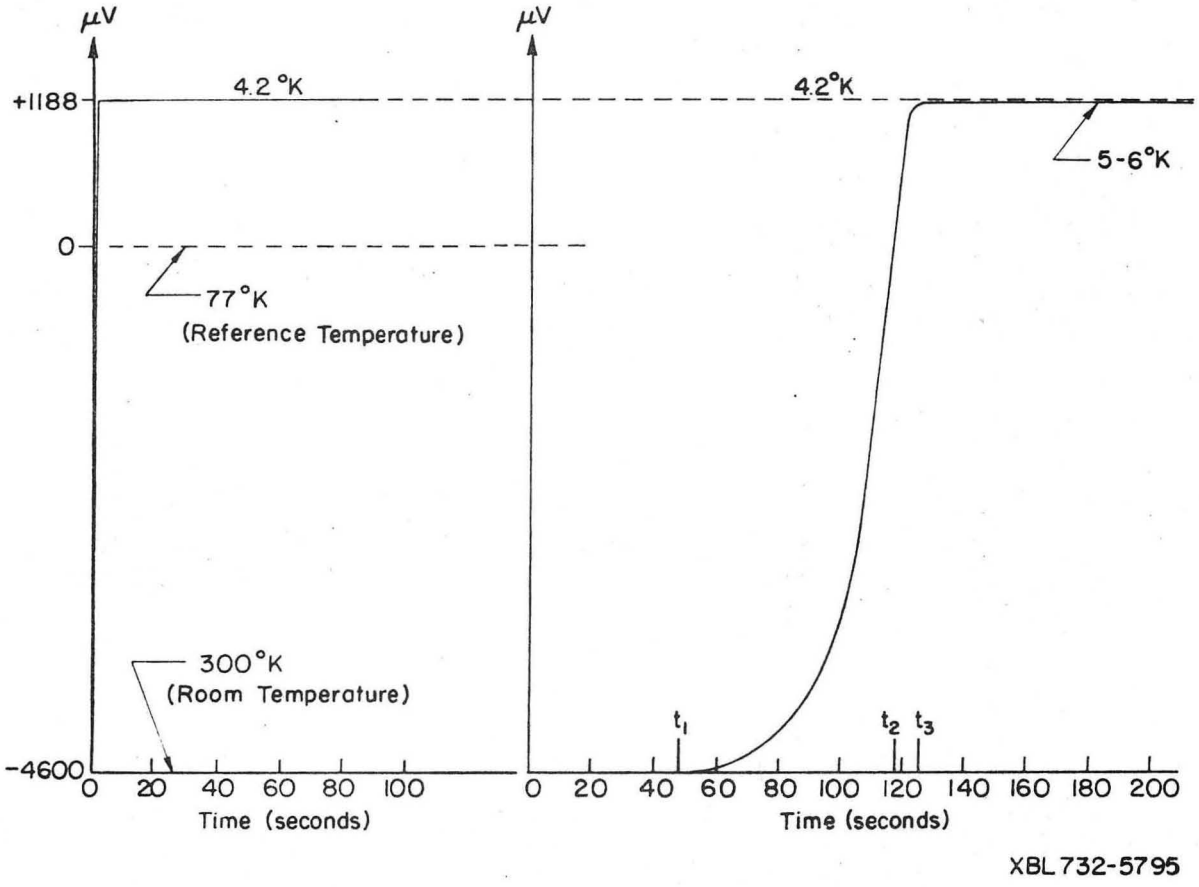
μV
+1188
4.2 °K
0
77°K
(Reference Temperature)
300°K
(Room Temperature)
-4600
0 20 40 60 80 100
Time (seconds)
μV
4.2°K
5-6°K
t1
t2 t3
0 20 40 60 80 100 120 140 160 180 200
Time (seconds)
XBL 732-5795

Fig. 18.

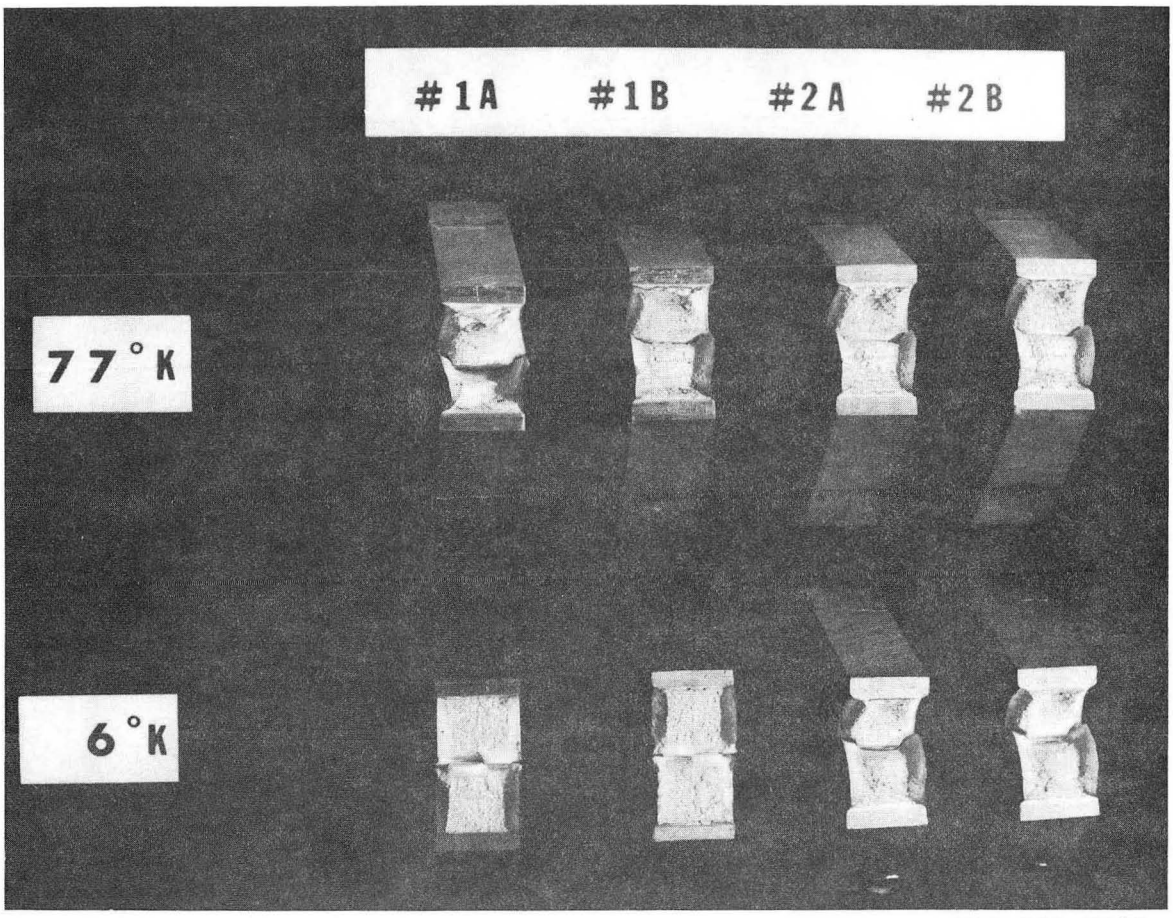

XBB 739-5645

Fig. 19.

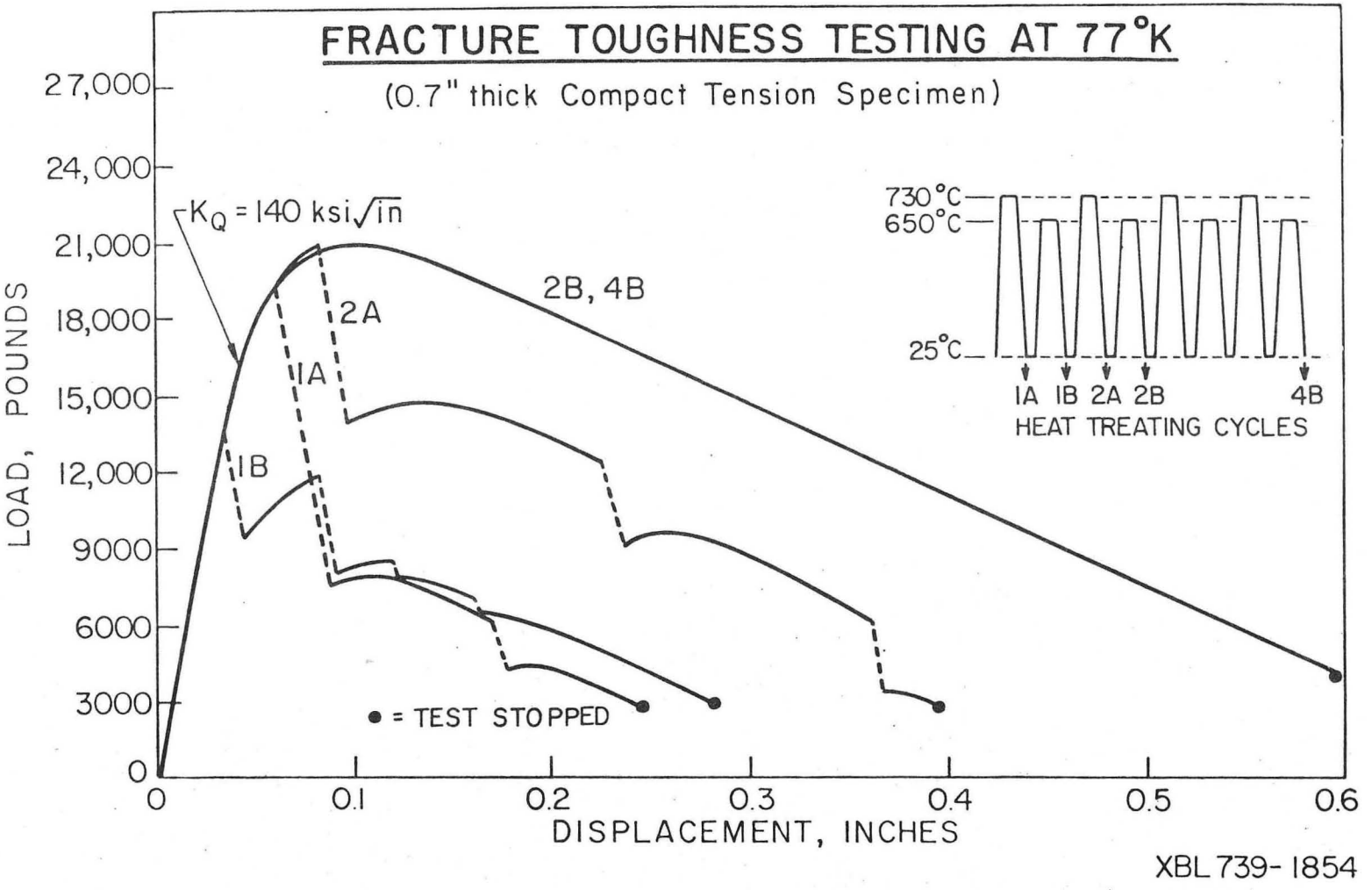
FRACTURE TOUGHNESS TESTING AT 77°K
(0.7" thick Compact Tension Specimen)
LOAD, POUNDS
27,000
24,000
21,000
18,000
15,000
12,000
9000
6000
3000
0
K_Q = 140 ksi$\sqrt{in}$
2B, 4B
2A
1A
1B
● = TEST STOPPED
730°C
650°C
25°C
1A 1B 2A 2B 4B
HEAT TREATING CYCLES
0
0.1
0.2
0.3
0.4
0.5
0.6
DISPLACEMENT, INCHES
XBL 739-1854

Fig. 20.

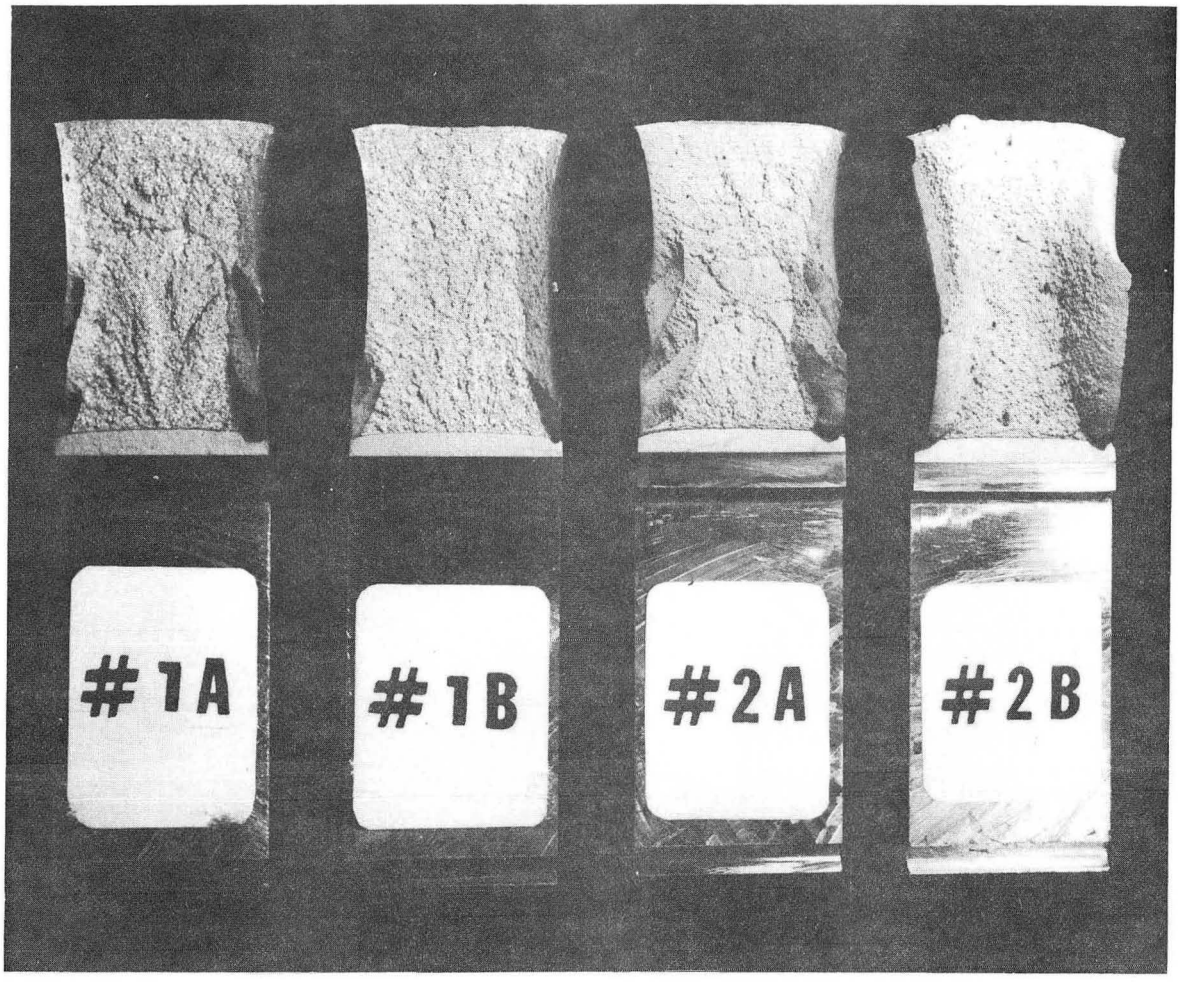

XBB 739-5644

Fig. 21.

FRACTOGRAPHS

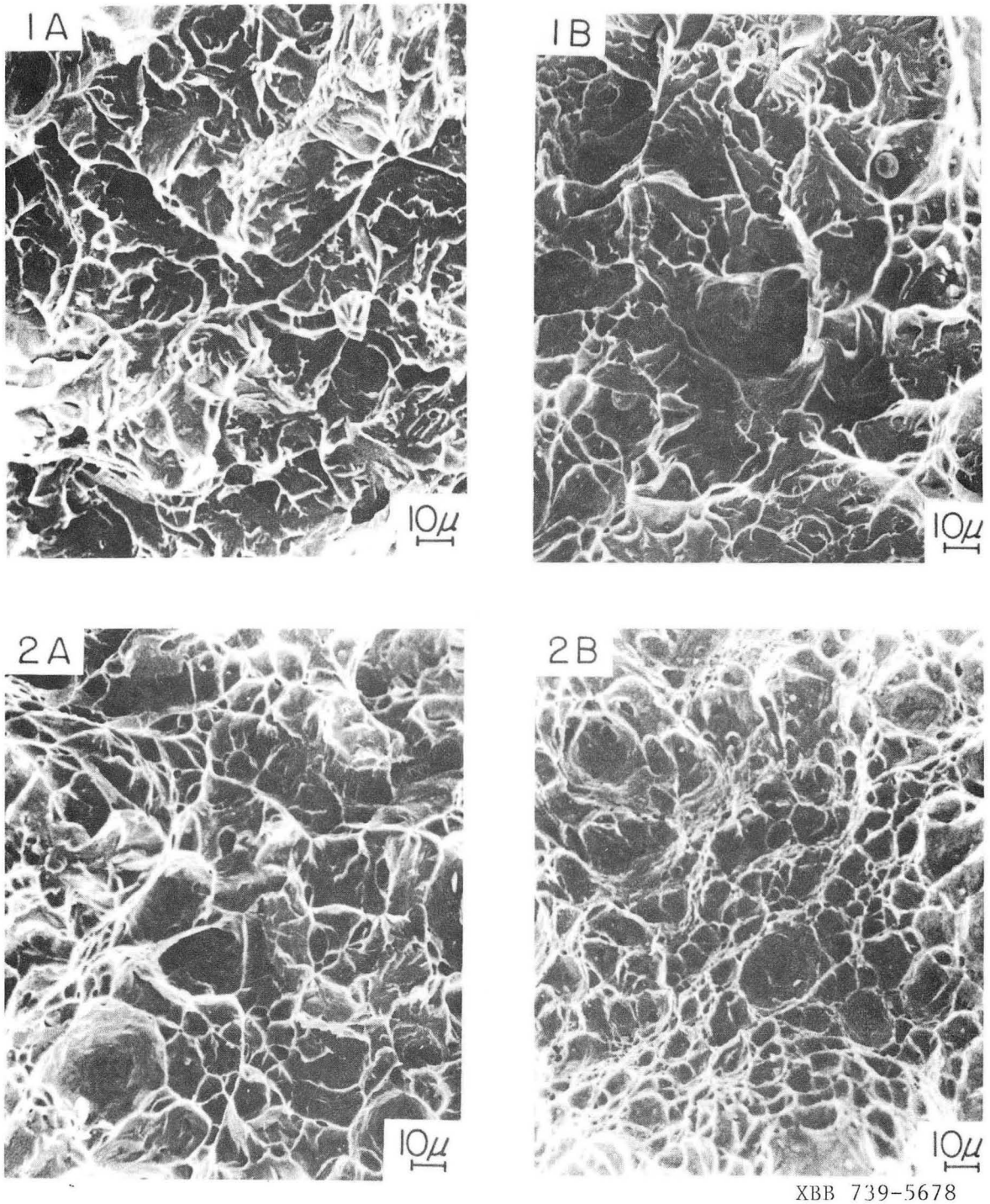

XBB 739-5678

Fig. 22.

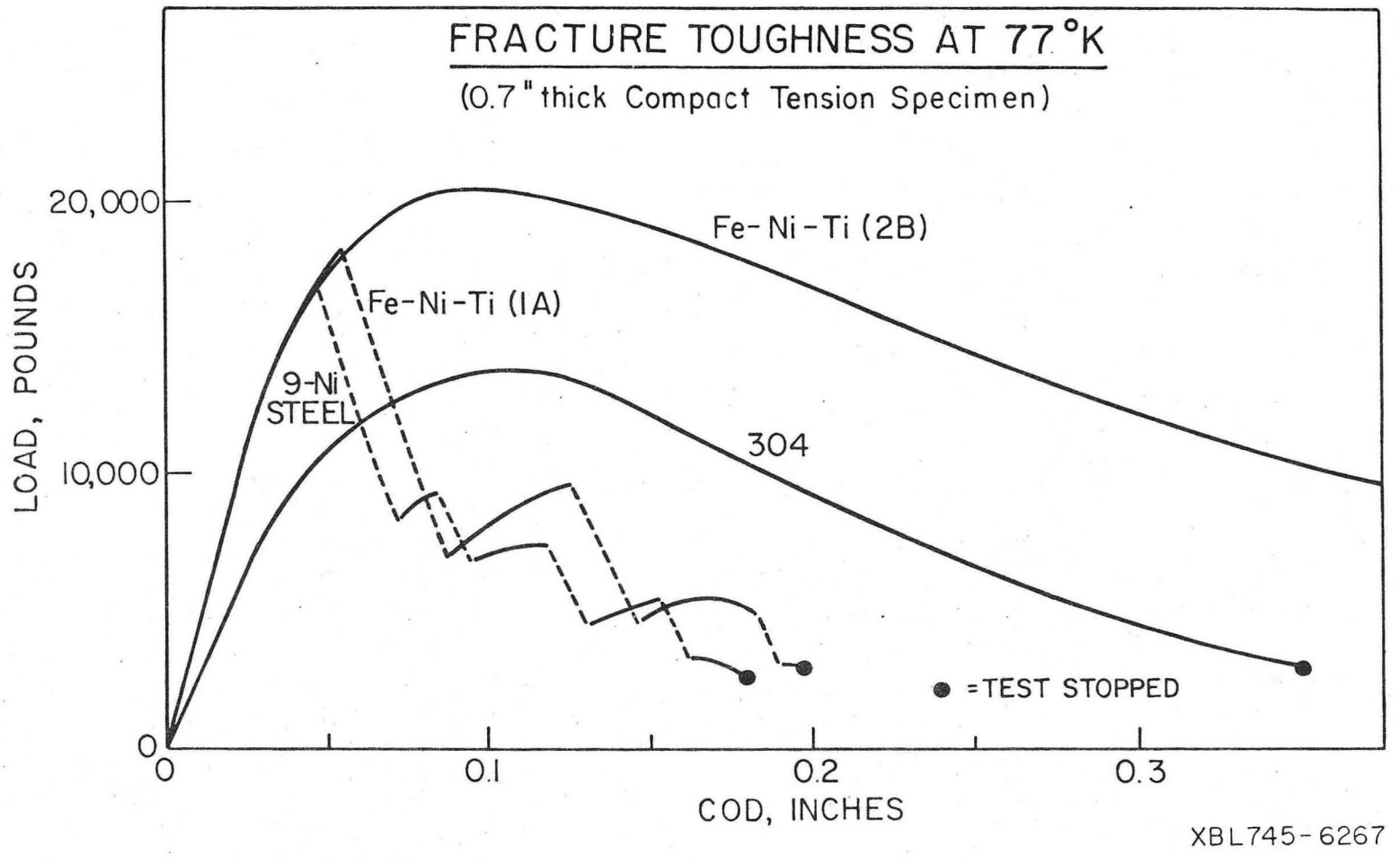
FRACTURE TOUGHNESS AT 77°K
(0.7" thick Compact Tension Specimen)
LOAD, POUNDS
20,000
10,000
0
0
0.1
0.2
0.3
COD, INCHES
Fe-Ni-Ti (2B)
Fe-Ni-Ti (1A)
9-Ni STEEL
304
● =TEST STOPPED
XBL745-6267

Fig. 23.

77°K

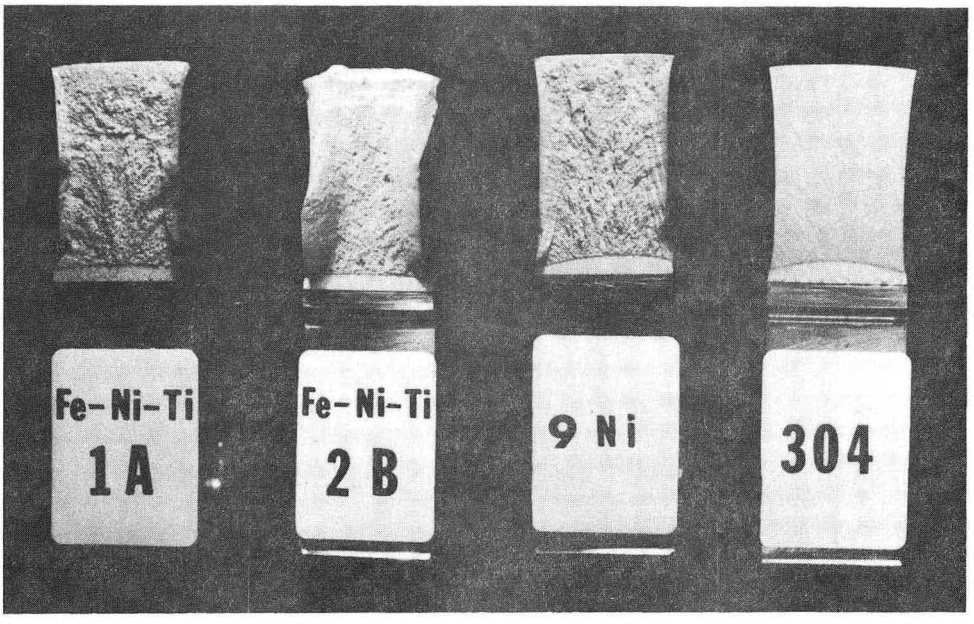

Fig. 24(a).

6°K

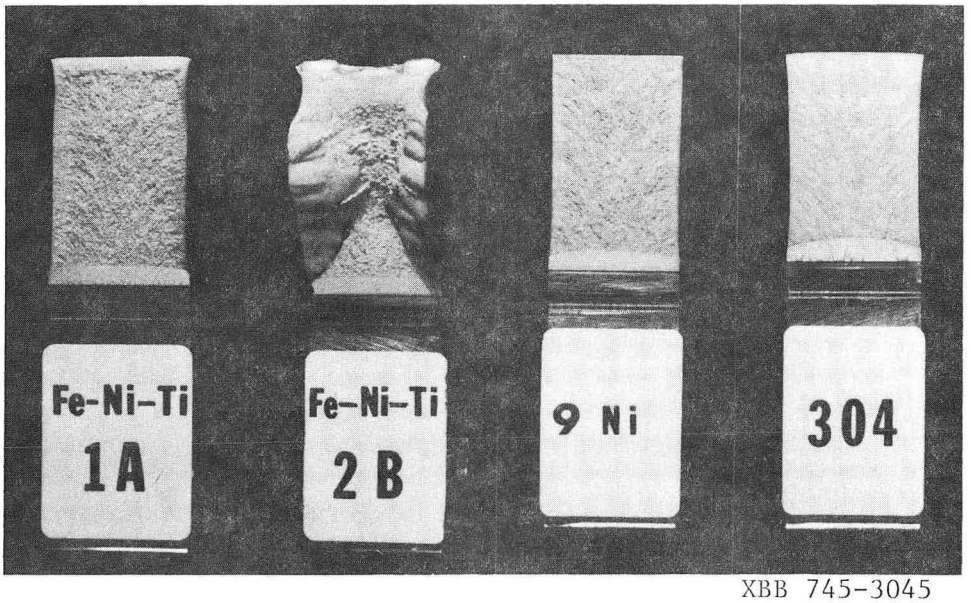

XBB 745-3045

Fig. 24(b).

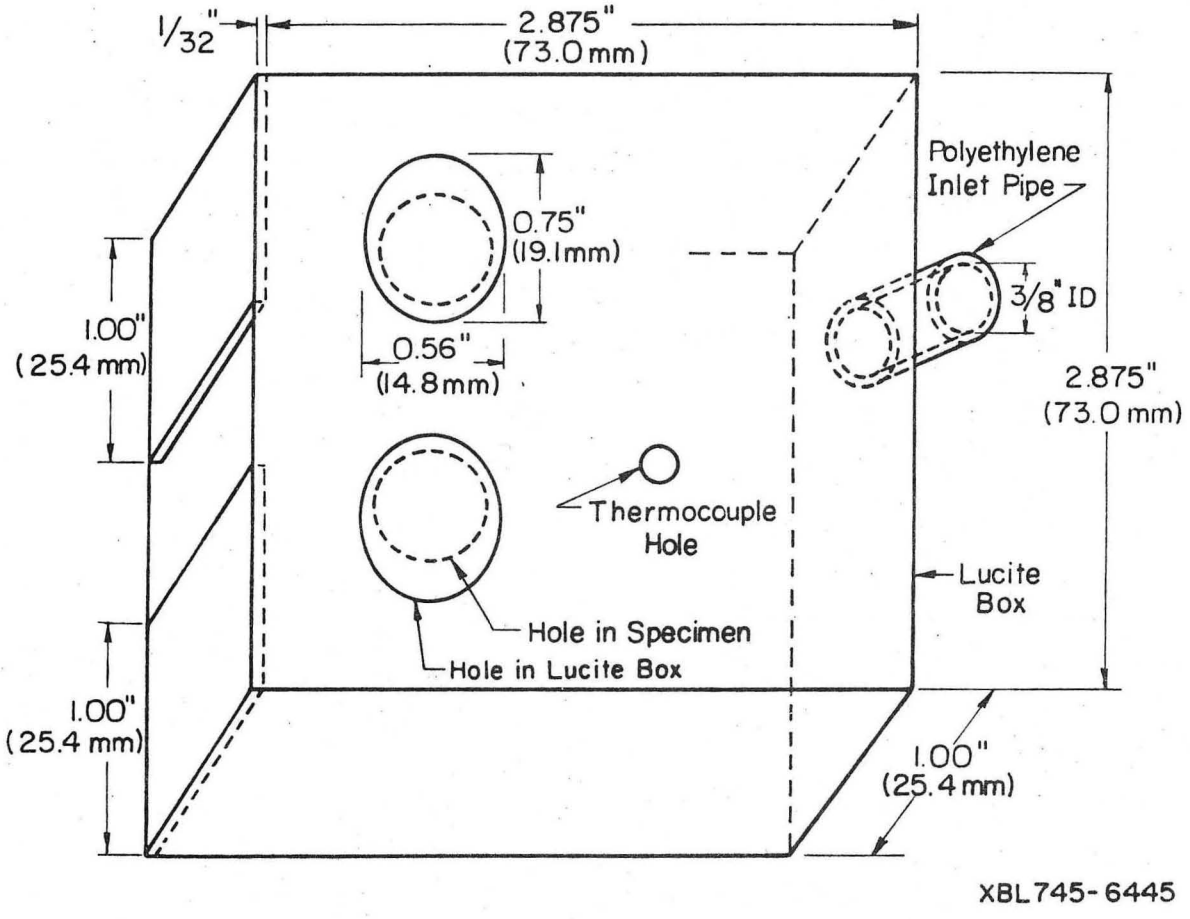
1/32"
2.875"
(73.0 mm)
Polyethylene
Inlet Pipe
0.75"
(19.1mm)
3/8" ID
1.00"
(25.4 mm)
0.56"
(14.8mm)
2.875"
(73.0 mm)
Thermocouple
Hole
Lucite
Box
Hole in Specimen
Hole in Lucite Box
1.00"
(25.4 mm)
1.00"
(25.4 mm)
XBL745-6445

Fig. 25.

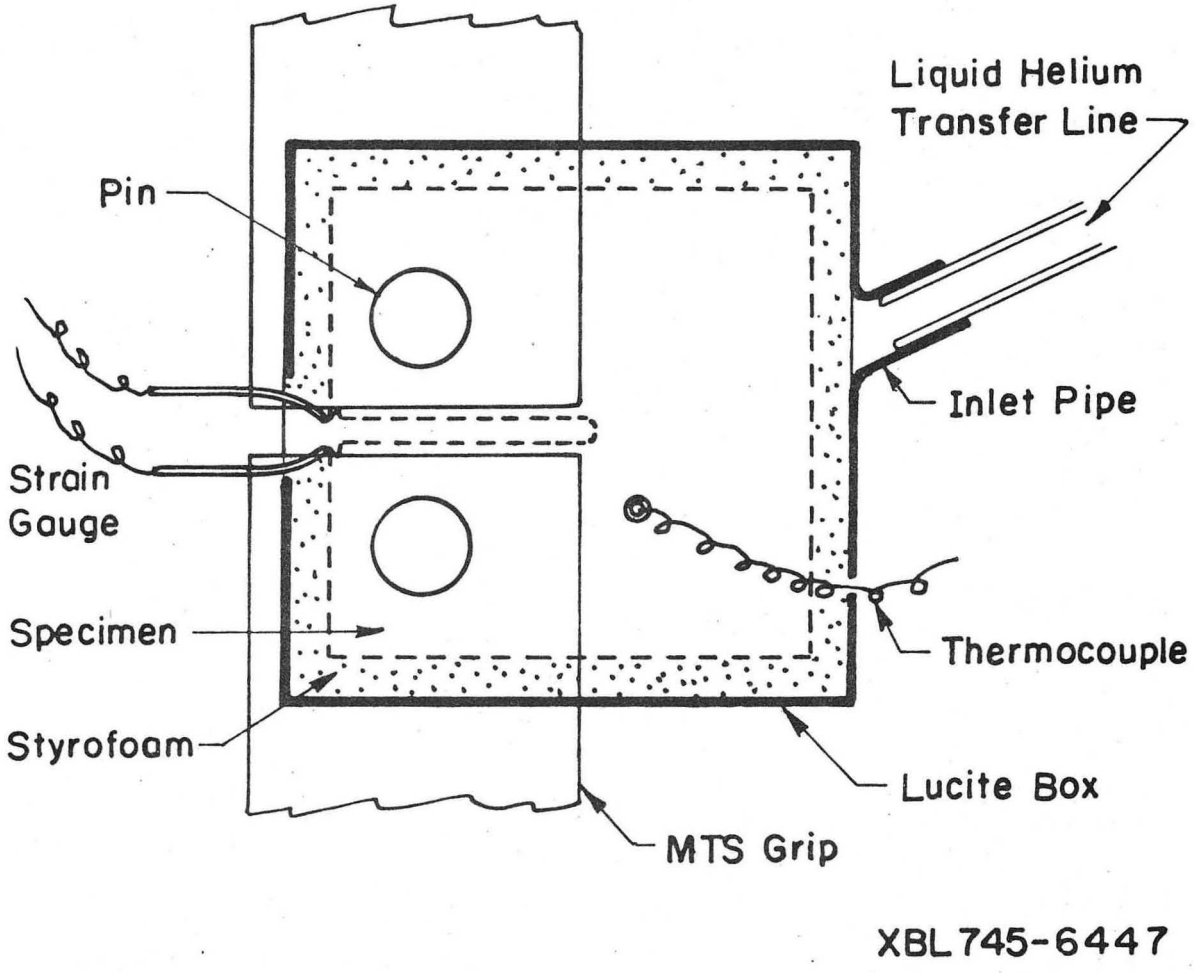
Liquid Helium
Transfer Line
Pin
Inlet Pipe
Strain
Gauge
Specimen
Thermocouple
Styrofoam
Lucite Box
MTS Grip
XBL745-6447

Fig. 26.

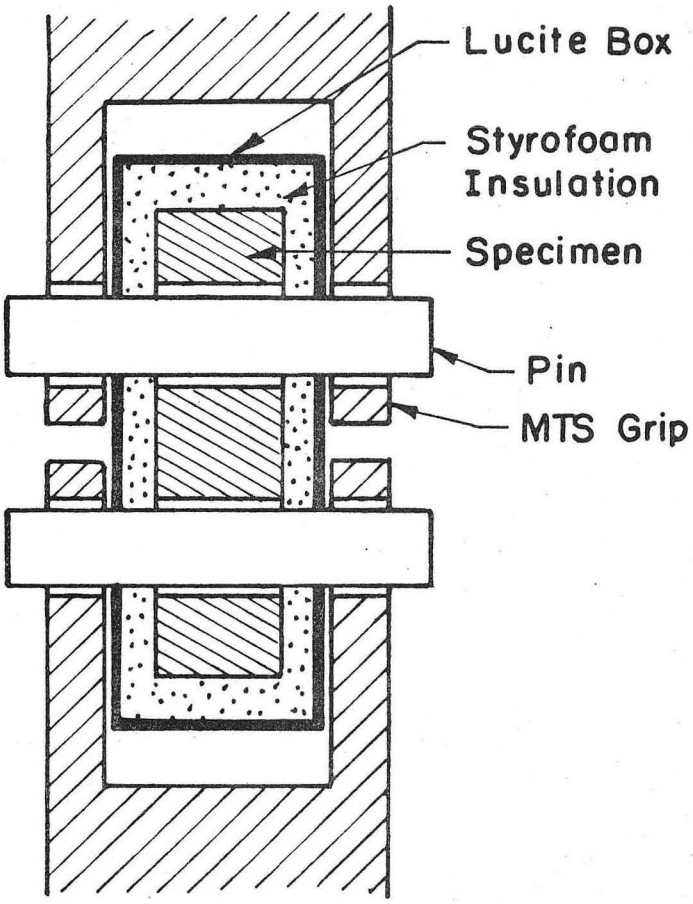

XBL 745-6446

Fig. 27.

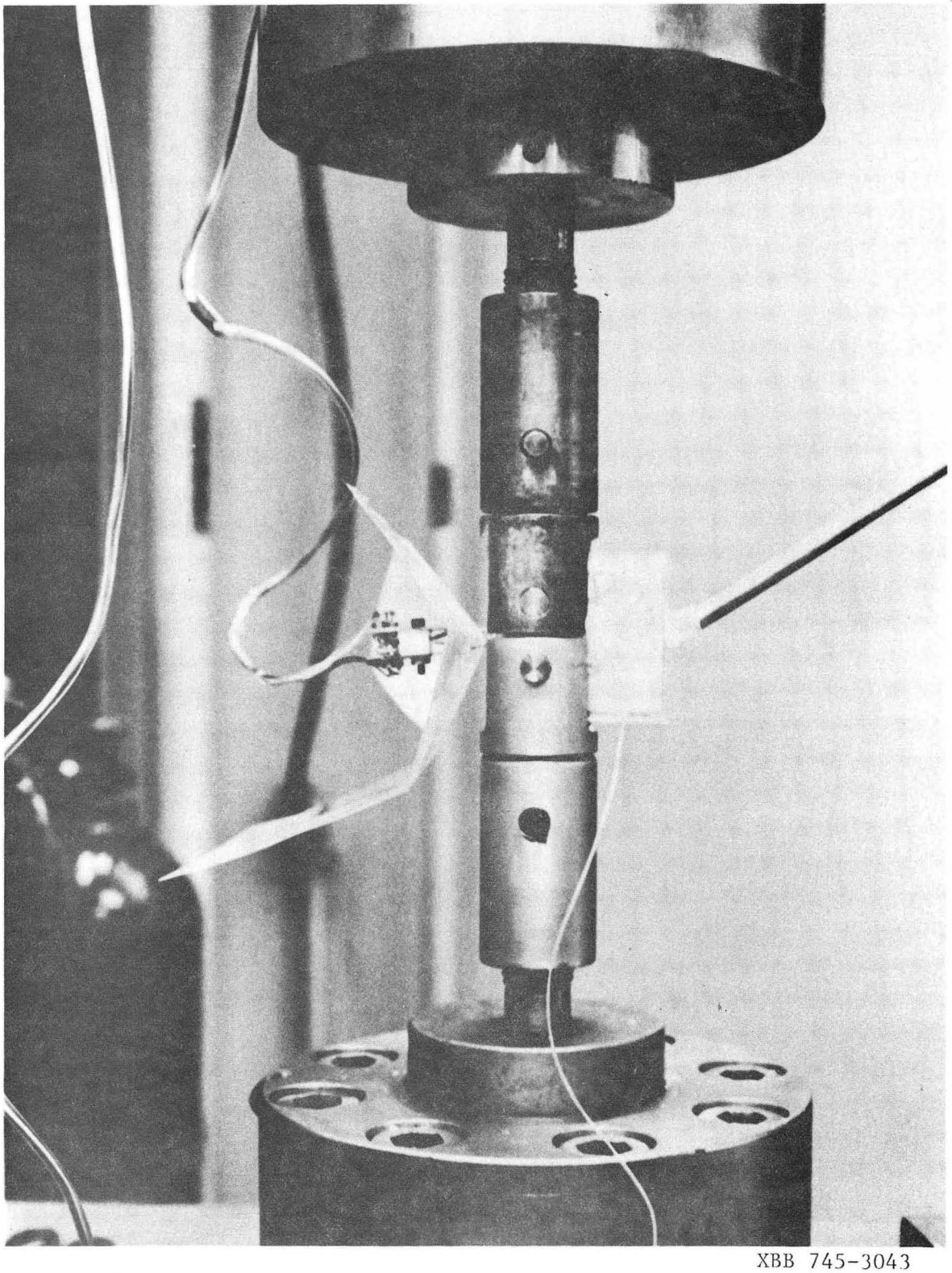

XBB 745-3043

Fig. 28(a).

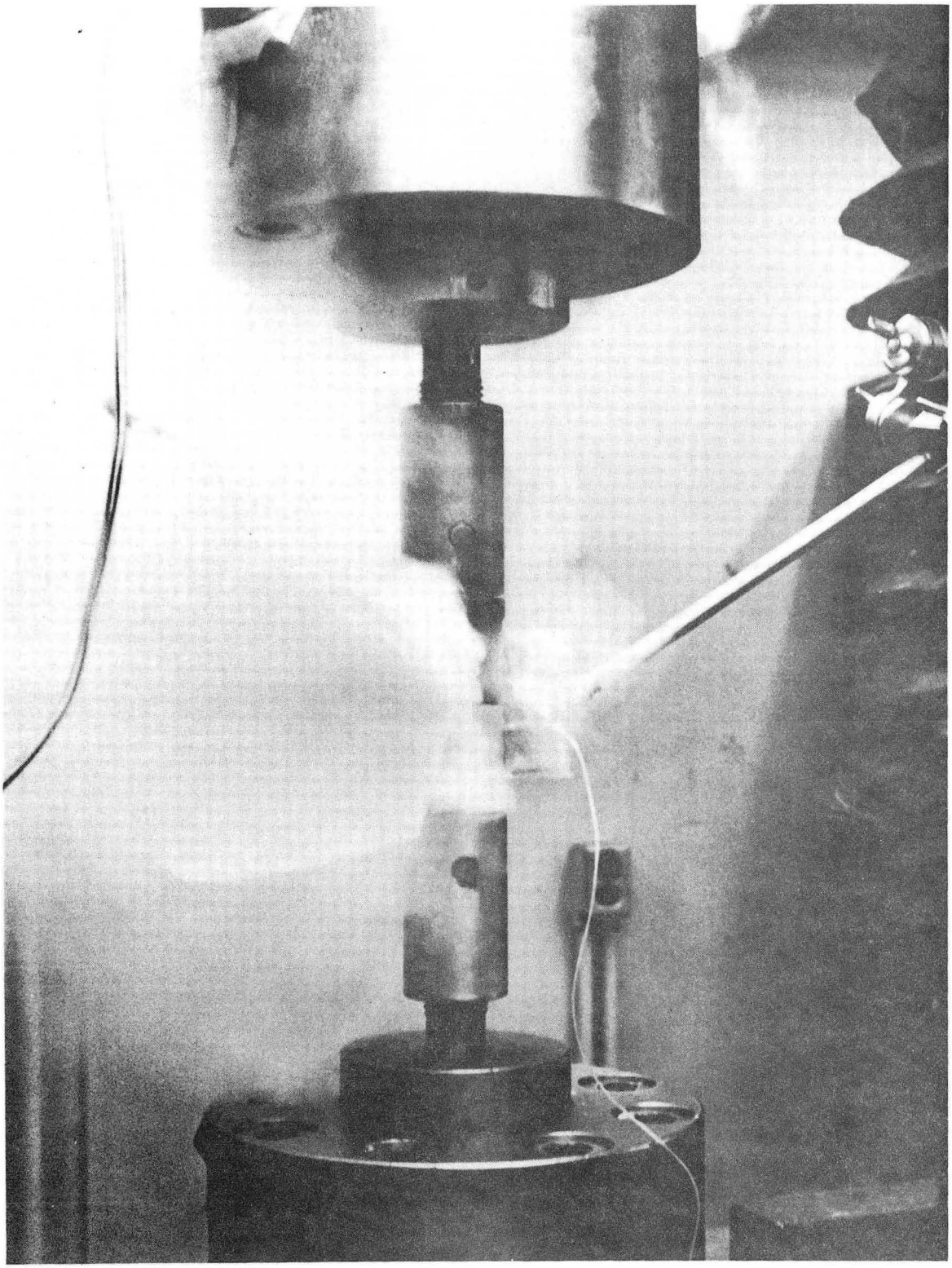

XBB 745-3042

Fig. 28(b).

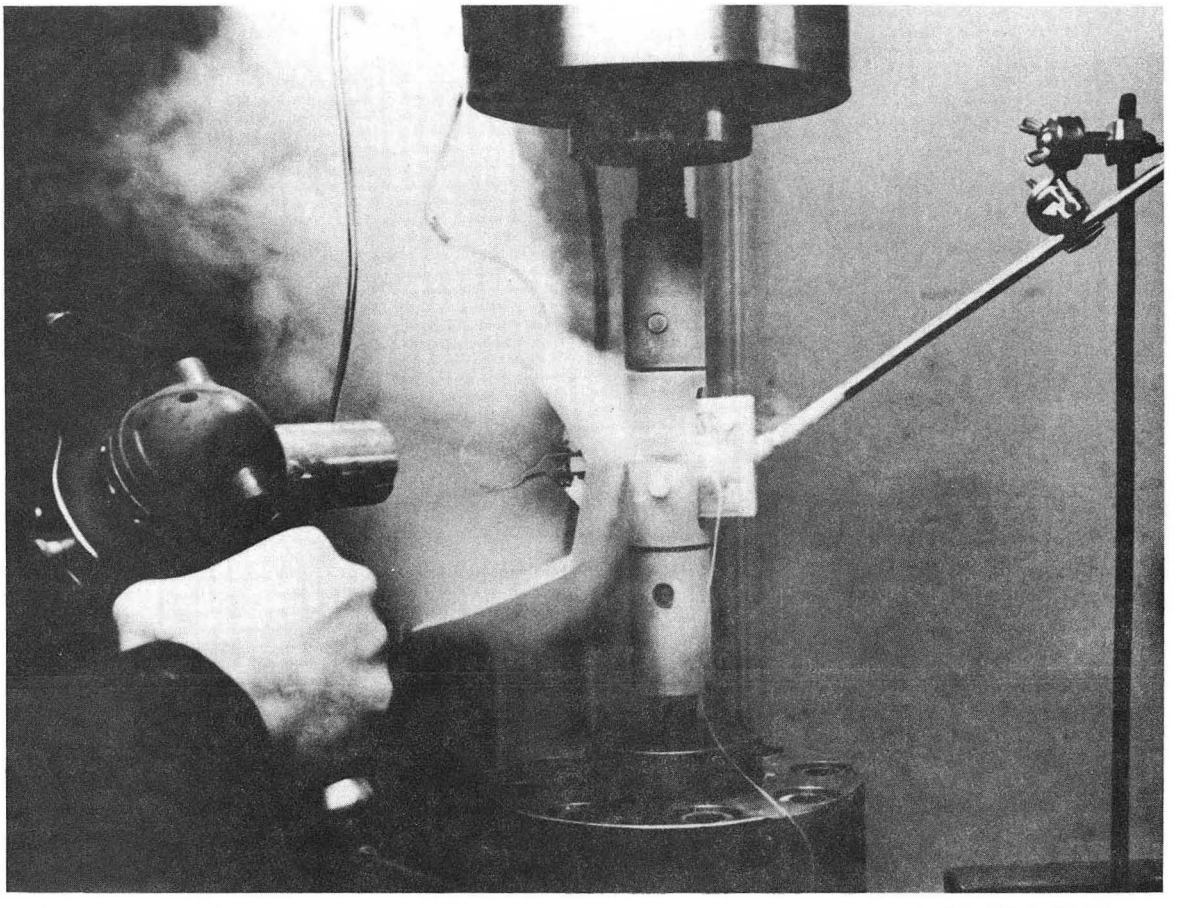

XBB 745-3044

Fig. 28(c).

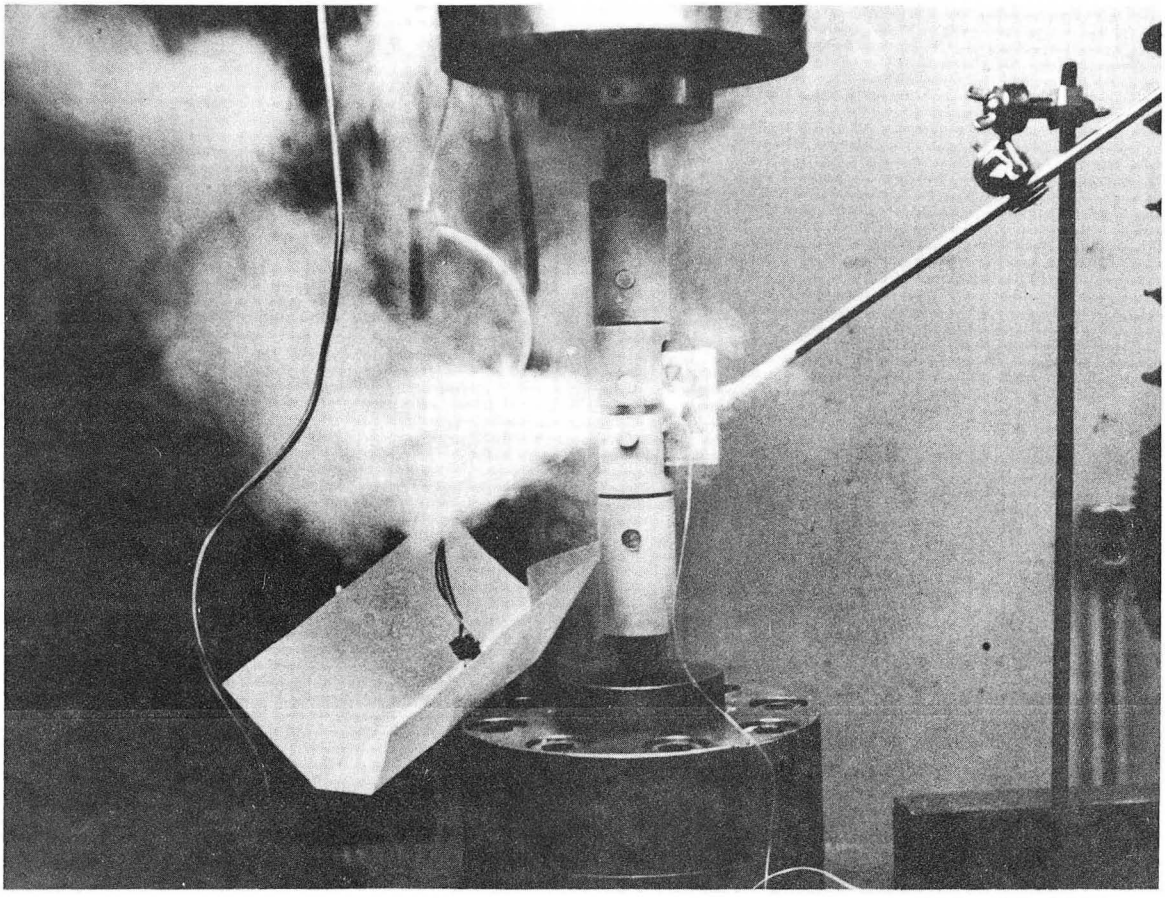

XBB 745-3041

Fig. 28(d).

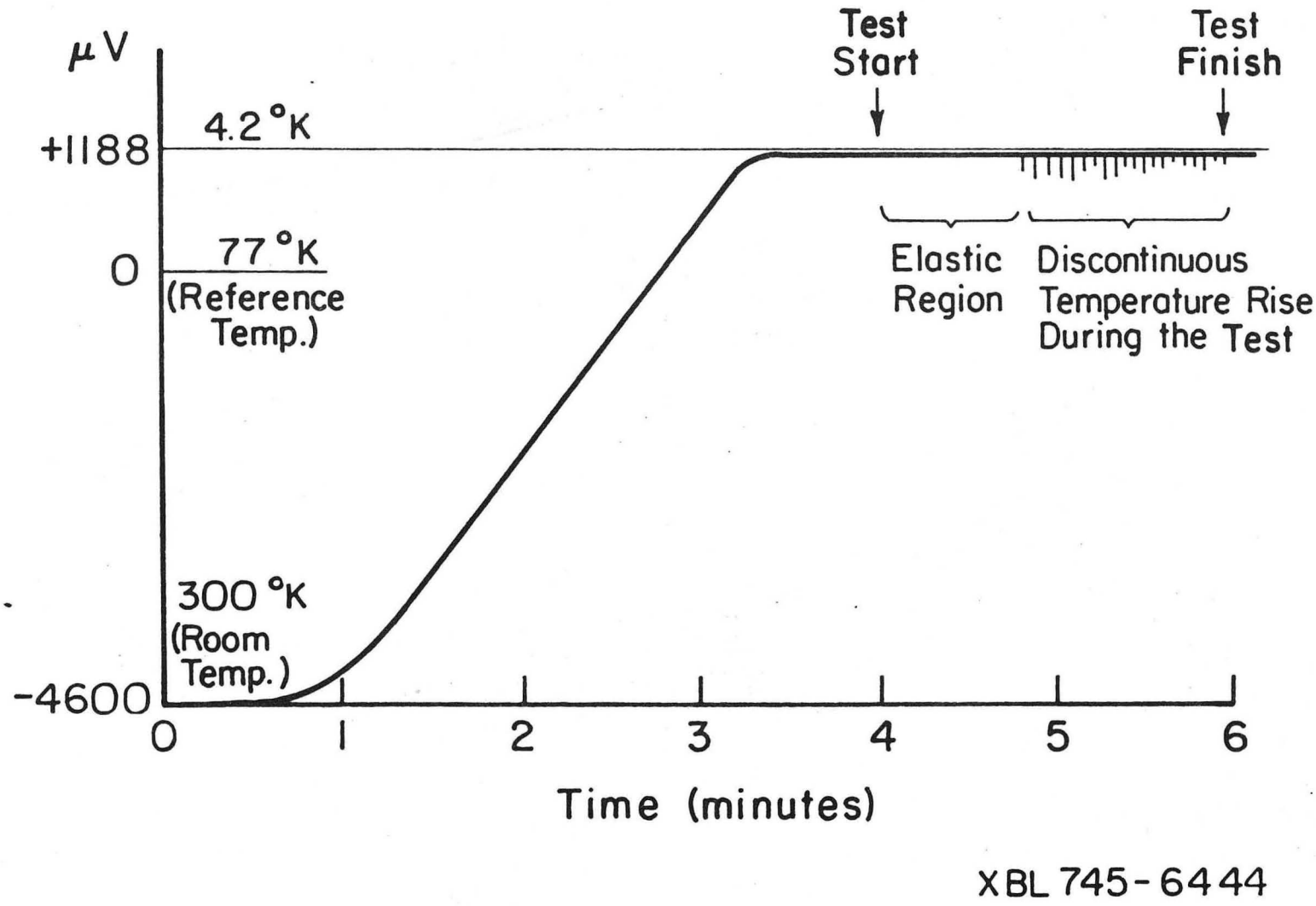
μV
+1188
0
-4600
4.2 °K
77 °K
(Reference
Temp.)
300 °K
(Room
Temp.)
Test
Start
Test
Finish
Elastic
Region
Discontinuous
Temperature Rise
During the Test
0
1
2
3
4
5
6
Time (minutes)
XBL 745-6444

Fig. 29.

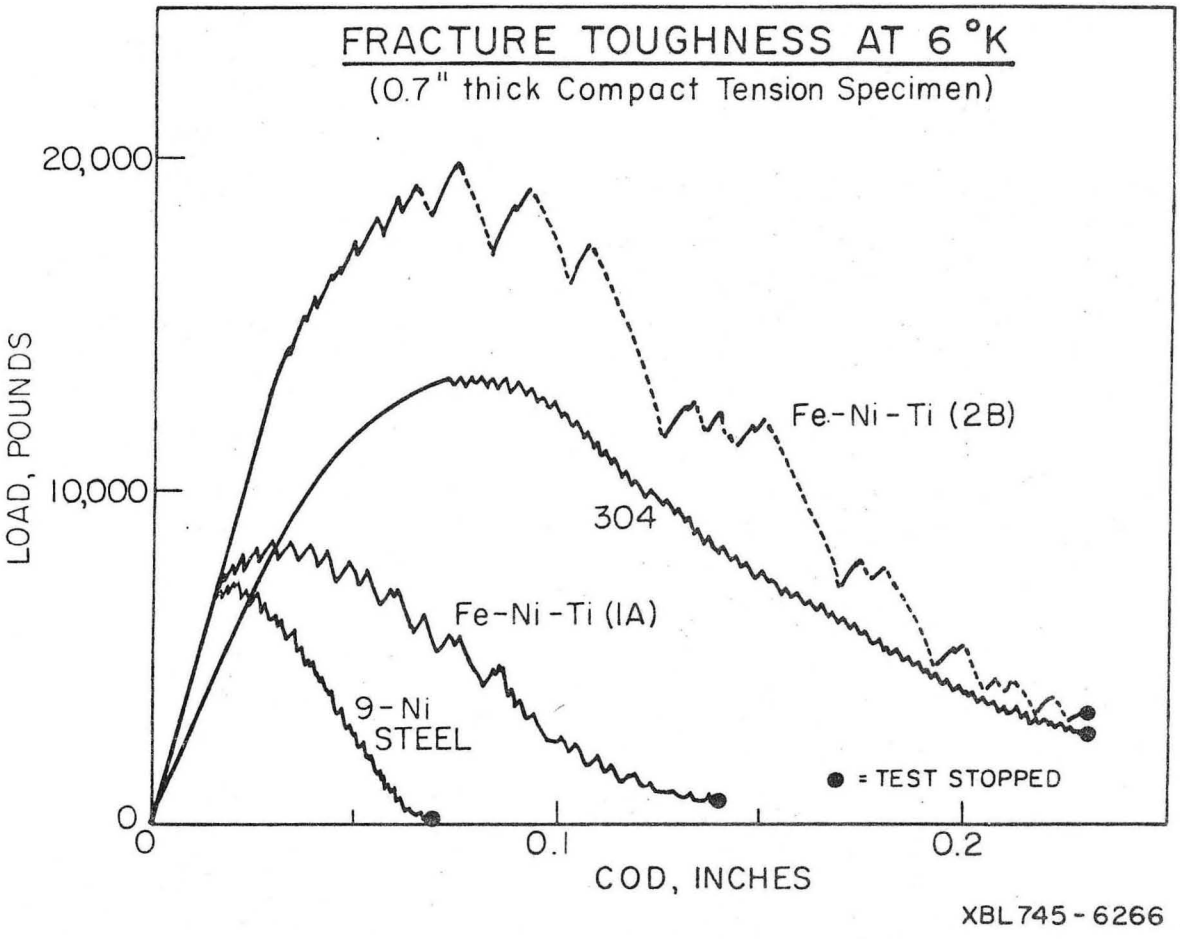
FRACTURE TOUGHNESS AT 6 °K
(0.7" thick Compact Tension Specimen)
20,000
10,000
0
LOAD, POUNDS
Fe-Ni-Ti (2B)
304
Fe-Ni-Ti (IA)
9-Ni
STEEL
● = TEST STOPPED
0
0.1
0.2
COD, INCHES
XBL745-6266

Fig. 30.

FRACTOGRAPHS

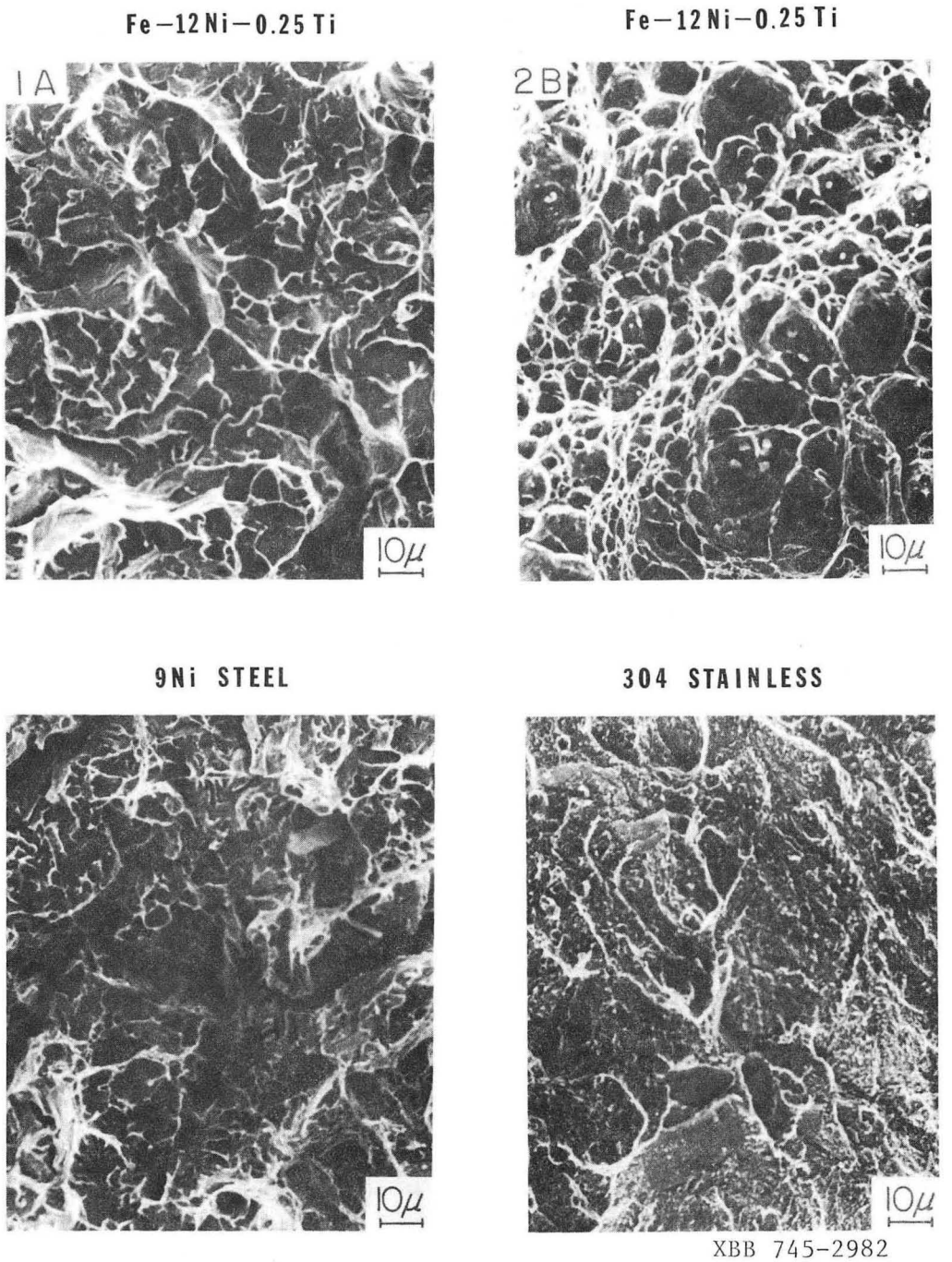

Fig. 31.

TECHNICAL INFORMATION DIVISION
LAWRENCE BERKELEY LABORATORY
UNIVERSITY OF CALIFORNIA
BERKELEY, CALIFORNIA 94720